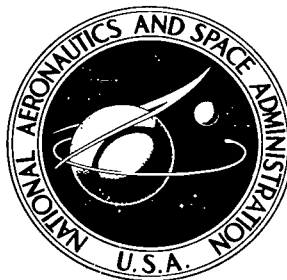


NASA TECHNICAL NOTE



NASA TN D-6067

e.1

LOAN COPY: RET  
AFWL (WLO1  
KIRTLAND AFB,



NASA TN D-6067

JET-WAKE EFFECT OF A HIGH-BYPASS ENGINE  
ON WING-NACELLE INTERFERENCE DRAG  
OF A SUBSONIC TRANSPORT AIRPLANE

*by James C. Patterson, Jr., and Stuart G. Flechner*

*Langley Research Center*

*Hampton, Va. 23365*

*Completed  
21 Oct 71 SW*

ERRATA

NASA Technical Note D-6067

JET-WAKE EFFECT OF A HIGH-BYPASS ENGINE ON WING-NACELLE  
INTERFERENCE DRAG OF A SUBSONIC TRANSPORT AIRPLANE

By James C. Patterson, Jr., and Stuart G. Flechner

November 1970

Page 45: The key of figure 15 is incorrect. The data for the short-duct flow-through nacelle should be indicated by the triangle symbol and the data for the long-duct flow-through nacelle should be indicated by the diamond symbol.



0132803

1. Report No. NASA TN D-6067	2. Government Accession No.	3. recipient's Catalog No.	
4. Title and Subtitle JET-WAKE EFFECT OF A HIGH-BYPASS ENGINE ON WING-NACELLE INTERFERENCE DRAG OF A SUBSONIC TRANSPORT AIRPLANE		5. Report Date November 1970	6. Performing Organization Code
		8. Performing Organization Report No. L-7310	10. Work Unit No. 737-01-10-01
7. Author(s) James C. Patterson, Jr., and Stuart G. Flechner		11. Contract or Grant No.	13. Type of Report and Period Covered Technical Note
9. Performing Organization Name and Address NASA Langley Research Center Hampton, Va. 23365		14. Sponsoring Agency Code	
		12. Sponsoring Agency Name and Address National Aeronautics and Space Administration Washington D.C. 20546	
15. Supplementary Notes			
16. Abstract  An experimental wind-tunnel investigation has been conducted recently by the National Aeronautics and Space Administration to determine the aerodynamic interference associated with the wing, pylon, and high-bypass fan-jet engines installed on a typical high-wing logistics transport airplane configuration and the interference due to the jet wake produced by powered model fan-jet engines. These tests were conducted over a Mach number range from 0.700 to 0.825 at angles of attack from 0° to 4°.			
17. Key Words (Suggested by Author(s)) Interference drag Fan-jet wake effect Engine-wake simulation		18. Distribution Statement Unclassified - Unlimited	
19. Security Classif. (of this report) Unclassified	20. Security Classif. (of this page) Unclassified	21. No. of Pages 45	22. Price* \$3.00

# JET-WAKE EFFECT OF A HIGH-BYPASS ENGINE ON WING-NACELLE INTERFERENCE DRAG OF A SUBSONIC TRANSPORT AIRPLANE

By James C. Patterson, Jr., and Stuart G. Flechner  
Langley Research Center

## SUMMARY

An experimental wind-tunnel investigation has been conducted by the National Aeronautics and Space Administration to determine the aerodynamic interference associated with the wing, pylon, and high-bypass fan-jet engines installed on a typical high-wing logistics transport airplane configuration and the interference due to the jet wake produced by powered model fan-jet engines. The most favorable longitudinal and vertical engine position was also to be determined for the type of propulsion system installation employed by this type of aircraft.

The data indicate that at the design cruise lift coefficient and Mach number, favorable aerodynamic interference drag was produced by properly positioning the pylon-mounted engines plus the favorable interference effect of the engine jet wake. The largest favorable interference values for this airplane were obtained with the engine in the most forward and lowest vertical position relative to the wing.

## INTRODUCTION

The present investigation of a four-engine high-wing airplane configuration is part of a wing-pylon-engine aerodynamic-interference program and is a continuation of an earlier interference investigation conducted on a similar two-engine cargo airplane. The results obtained during the earlier investigation, conducted primarily to determine whether such large engines would cause severe adverse interference, are reported in reference 1. These results indicate that the interference drag may be favorable for the proposed type of underwing engine-pylon installation because of the reduction in induced drag associated with an underwing fence effect of the nacelle-pylon combination. It is also shown that engine wake as well as the longitudinal and vertical positioning of the engine relative to the wing, has a strong influence on this aerodynamic interference phenomenon.

In the present investigation, as in the earlier investigation, the jet wake is simulated by model fan-jet engines capable of producing the same relative mass-flow rate and fan-exit pressure ratio as a representative full-scale high-bypass-ratio fan-jet engine. This

investigation was conducted by use of a semispan model of a logistics transport airplane configuration with two model fan-jet engines pylong-mounted under the wing at various longitudinal and vertical positions. These tests were conducted over the Mach number range from 0.700 to 0.825 at angles of attack from  $0^{\circ}$  to  $4^{\circ}$ , which includes the cruise Mach number of 0.775 and lift coefficient of 0.5.

#### SYMBOLS

A	area, meters <sup>2</sup>
(A) <sub>wet</sub>	wetted area, meters <sup>2</sup>
C <sub>D</sub>	drag coefficient, Drag/ $q_{\infty}S$
$\Delta C_D$	interference-drag coefficient
C <sub>F,n</sub>	net-thrust coefficient
C <sub>f</sub>	friction coefficient
C <sub>L</sub>	lift coefficient, Lift/ $q_{\infty}S$
C <sub>p</sub>	pressure coefficient, $\frac{p_l - p_{\infty}}{q_{\infty}}$
$\Delta C_p$	differential pressure coefficient
c	chord, meters
$\bar{c}$	mean geometric chord, 53.741 centimeters
D <sub>r</sub>	ram drag, newtons
D <sub>s</sub>	scrubbing drag, newtons
F <sub>g,f</sub>	fan gross thrust, newtons
F <sub>g,p</sub>	primary gross thrust, newtons
F <sub>n</sub>	net thrust, newtons

K	fan-inlet mass-flow rate correction from ASME nozzle calibration
M	Mach number
$\dot{m}$	mass-flow rate, kilograms/second
p	pressure, newtons/meter <sup>2</sup>
q	dynamic pressure, newtons/meter <sup>2</sup>
R	specific gas constant (for air, 0.2871 joule/ <sup>o</sup> K-mole; for nitrogen, 0.2968 joule/ <sup>o</sup> K-mole), joules/ <sup>o</sup> K-mole
S	semispan wing area, 0.936 meter <sup>2</sup>
T	absolute temperature, <sup>o</sup> K
V	velocity, meters/second
x	longitudinal distance, meters
$\alpha$	angle of attack, degrees
$\gamma$	specific heat ratio (for air, 1.40; for nitrogen 1.41)
$\rho$	density, kilograms/meter <sup>3</sup>

Subscripts:

av	average
e	exit
i	inlet
l	local
p	primary or turbine
st	static

t            total  
 $\infty$          free stream

## APPARATUS AND EXPERIMENTAL METHODS

### Test Facility

The investigation was conducted in the Langley 8-foot transonic pressure tunnel. The rectangular test section has a longitudinally slotted floor and ceiling and solid side walls, as shown in figure 1. The slots reduce the wall interference; thus, relatively large models can be tested through the subsonic speed range. (See ref. 2.) The model used in this investigation has a ratio of wing semispan to tunnel width of 0.82, and a ratio of model frontal area to tunnel test-section area of 0.049. The change in Mach number resulting from tunnel blockage is 0.0005, which is well within the Mach number accuracy of 0.002.

### Model Configuration

Drawings of the semispan model and engine nacelle are shown in figure 2. A photograph of the model installed in the wind tunnel is shown in figure 3. Model coordinates are given in table I.

Wing and fuselage.- The semispan aluminum wing shown in figure 2 has a quarter-chord sweep of approximately  $24^{\circ}$ , an aspect ratio of 7.1, a taper ratio of 0.372, and a twist distribution from  $0^{\circ}$  at the wing root to  $-1.50^{\circ}$  at the 0.82-meter station and  $-3.50^{\circ}$  at the tip. The airfoil coordinates for these stations are given in table I.

The model wing has a semispan of 1.788 meters, which simulates the inboard 94 percent of a higher-aspect-ratio (7.750) model wing having a semispan of 1.904 meters. Removal of the outboard part of the wing, which was necessary because of test-facility model-size restrictions, should not significantly affect the wing-pylon-nacelle interference phenomena with the nacelles in their relatively inboard locations of 69.5 and 108.1 cm from the fuselage center line.

The fuselage has the profile of a typical C-5A type logistics transport airplane. The nose and afterbody of the fuselage are constructed of wood; the midsection is removable.

Engine and pylon.- A cross-sectional view of the powered fan-jet engine used in this investigation is shown in figure 4. The two-stage model fan is connected directly to a three-stage turbine, which is driven by compressed gas. The model engine simulates the same relative mass-flow ratio of an actual engine with a bypass ratio of 8 and fan-exit total-pressure ratio of 1.5 at the model-engine design maximum rotational speed of

approximately 45 000 rpm. In addition to the powered engine, data were also obtained with two different flow-through-nacelle configurations. One flow-through-nacelle configuration simulates the powered engine with a short-duct fan forward of the turbine and with the same overall external lines as the powered nacelle. A second flow-through-nacelle configuration with the same fan-cowl contours but with an extension of the fan exit to approximately the turbine exit location of the powered nacelle was also tested. (See fig. 5.)

Tests were conducted with the engines in four positions, two longitudinal and two vertical locations relative to the wing as shown in figure 5. The effects of extending the pylon leading edge and changing the pylon sweep and pylon thickness were also investigated.

Each pylon consists of a hollow steel structural member enclosed in an aluminum shell contoured to the desired airfoil shape. This support beam also serves as a path for the compressed gas from the wing to the powered model fan-jet engine. Coordinates for each pylon tested are given in table I. The long-duct flow-through nacelles also shown in figure 5 were tested on a set of constant-chord pylons constructed of solid aluminum.

To obtain data for the engine alone, the powered model fan-jet engine was installed in the wind tunnel on a specially designed elongated pylon, as shown in figure 6.

#### Driving-Gas System

Nitrogen was used as a clean, dry, economical model-engine driving fluid, and each engine was individually controlled in a manner similar to that of reference 1. A dual control system was necessary to insure equal thrust output from each engine in spite of any dissimilarities that might exist between the two engines and to obtain a constant total thrust output for each configuration tested, a necessity in the analysis of the results obtained with the various pylon configurations. The introduction of nitrogen into the wind-tunnel flow is considered to have little or no effect on the stream characteristics because of the similarity in the physical characteristics of nitrogen and air.

#### Instrumentation

Force balance.- Measurements of forces and moments were obtained from an internally mounted, wall-supported, five-component electrical strain-gage balance. The model was designed so that the wing was attached to the balance, but not to the fuselage, and protruded through a clearance opening in the fuselage. The fuselage, even though grounded to the tunnel wall, was attached to the balance wall-support system, which allowed the fuselage as well as the balance to traverse the angle-of-attack range.

Part of the fuselage was submerged in the tunnel boundary layer; therefore, any fuselage force measurements would be of no value. The effect of the fuselage flow field on the wing, pylon, and engine-nacelle forces, however, was present.

Surface pressure measurements.- The wing chordwise pressure distribution was measured on the lower surface approximately 2 cm inboard and outboard of each pylon. The pylon pressure distribution was measured at two vertical locations on each pylon. Pressure orifices were located horizontally at approximately one-eighth and one-half the pylon span. The constant-chord pylon used with the flow-through nacelle and the elongated pylon used during the engine-alone test were not instrumentated. Longitudinal rows of pressure orifices on the surface of the powered engine were located circumferentially at  $30^{\circ}$  and  $330^{\circ}$  around the fan and turbine cowls and at  $90^{\circ}$  and  $270^{\circ}$  on the turbine plug.

Engine internal measurements.- The total and static pressure and total temperature were measured in the fan inlet and exit and in the turbine inlet and exit to be used in computing thrust. The fan-inlet total pressure was measured with four total-pressure rakes located just forward of the first-stage fan rotor at the  $11^{\circ}$ ,  $148^{\circ}$ ,  $180^{\circ}$ , and  $240^{\circ}$  circumferential positions. (See fig. 4.) In addition to the pressure measurements obtained by the six probes on each, an assumption that free-stream total pressure exists midway between the innermost rake probe and the fan hub is also used in the thrust computation.

Five static-pressure orifices were located on the fan cowl inner surface circumferentially at  $0^{\circ}$ ,  $90^{\circ}$ ,  $164^{\circ}$ ,  $210^{\circ}$ , and  $270^{\circ}$ , and two static-pressure rakes were located circumferentially at  $128^{\circ}$  and  $350^{\circ}$ . The static-pressure-rake support strut has a symmetrical airfoil section,  $12^{\circ}$  leading-edge sweep, and a 1.767-cm mean chord. The static-pressure orifice on each of the three probes on each static-pressure rake is located 1.016 cm behind the rake trailing edge to allow the flow to return to free-stream conditions before the static-pressure measurement is made.

There are seven total-pressure rakes at the fan exit located circumferentially at  $27^{\circ}$ ,  $78^{\circ}$ ,  $129^{\circ}$ ,  $183^{\circ}$ ,  $231^{\circ}$ ,  $282^{\circ}$ , and  $333^{\circ}$ . Each total-pressure rake has five probes spaced radially so that each probe was centered in one of five concentric circular equal-area segments. These areas were then equally divided circumferentially among the seven rakes. The result is an equal weighing factor for each probe. A thermocouple probe was installed on each of the fan-exit total-pressure rakes, located radially at a position approximately equidistant from the inner fan cowl and the outer turbine cowl surfaces.

Just inside the fan exit, on the inner side of the cowl and on the turbine cowl surface, static-pressure orifices were located at  $30^{\circ}$ ,  $90^{\circ}$ ,  $180^{\circ}$ ,  $270^{\circ}$ , and  $330^{\circ}$ . A linear static-pressure distribution from one surface to the other was assumed.

The turbine inlet flow conditions were obtained from a turbine-type flowmeter placed in the nitrogen supply line of each engine just prior to the entrance of the nitrogen

into the model. From the measurements of flowmeter turbine speed, the nitrogen pressure and temperature, and the meter volumetric flow calibration, the turbine inlet flow conditions were established. The turbine-type meter is very susceptible to damage from excessive or sudden load changes that may possibly alter the flowmeter turbine-blade pitch. To guard against this possibility, the flowmeters were recalibrated at the termination of the tunnel test. This calibration validated the pretest calibration.

The flow conditions existing at the turbine exit were obtained in a manner similar to that used at the fan exit, with three total-pressure rakes located at  $60^{\circ}$ ,  $183^{\circ}$ , and  $300^{\circ}$  and static-pressure orifices at  $90^{\circ}$ ,  $180^{\circ}$ , and  $270^{\circ}$ . Two thermocouple probes, at  $165^{\circ}$  and  $235^{\circ}$ , were located upstream of the total-pressure rakes.

Each long-duct flow-through nacelles had three static-pressure orifices just inside the nacelle exit. The orifices were located circumferentially at  $0^{\circ}$ ,  $120^{\circ}$ , and  $240^{\circ}$ .

Each short-duct flow-through nacelle had three static-pressure probes in the fan exit located 70 percent of the distance from the turbine surface to the inside fan cowl surface and three static-pressure orifices approximately 7.5 mm inside the center duct exit. The orifices and probes were located circumferentially at  $75^{\circ}$ ,  $195^{\circ}$ , and  $315^{\circ}$ .

All wing, pylon, engine surface, and engine internal pressure measurements were made with 12 pressure-scanning valves mounted inside the fuselage. Magnetic pickups were used to determine the fan-shaft rotational speed. All thermocouples were chromel-alumel, and the output was recorded by a potentiometer on a paper strip chart.

Calibration of model engine.- Because of the incompleteness of the flow surveys made in the fan inlet and exit, these measurements required calibration. The ASME flow nozzle (shown in ref. 1) was used for this purpose where the engine mass-flow rate could be determined from static-pressure measurements in the constant-area part of the nozzle, the ambient stagnation pressure and temperature, plus the ASME nozzle flow coefficient of 0.992. This value was then divided by the mass flow calculated from the fan-inlet measurements, and the resulting flow coefficient was used to correct the inlet mass-flow measurements made during the investigation.

### Test Conditions

Investigations were made of the complete wing-fuselage-pylon-engine configuration, the wing-fuselage configuration, and the engine alone. The engine for the engine-alone tests was mounted on an elongated pylon, which was attached directly to the wall-mounted force balance. Long- and short-duct nacelles were mounted on the wing-fuselage-pylon combination and on the elongated pylon.

The tunnel stagnation pressure was approximately  $96 \text{ kN/m}^2$  for this investigation because of the operating limits of the model engine and the nitrogen-supply valving system. The tunnel stagnation temperature was reduced from the normal operating temperature of  $322^\circ \text{ K}$  to  $311^\circ \text{ K}$ .

The engine was operated at fan-exit total-pressure ratios of 1.0 and 1.5. The fan-exit total-pressure ratio of 1.0 was obtained with the engine operating just fast enough to overcome the internal losses of the engine (approximately 22 000 rpm), and zero thrust was produced. A fan-exit total-pressure ratio of 1.5 was produced with the engine operating at the maximum design speed (45 000 rpm), where maximum thrust was produced.

For all configurations, boundary-layer transition strips, approximately 3 mm wide and consisting of No. 120 carborundum grains set in a plastic adhesive, were installed on the upper and lower wing surfaces and on the pylons at the 10-percent local-chord position. Transition on the fan cowl and on the flow-through nacelles was also fixed at a streamwise location approximately 13 mm from the inlet leading edge, on both the inside and the outside of the inlet.

The angle-of-attack range of  $0^\circ$  to  $4^\circ$  was covered at Mach numbers of 0.700, 0.750, 0.775, 0.800, and 0.825.

#### INTERFERENCE DRAG

To obtain the value of only interference drag resulting from the effect of both pylon-engine combinations in the presence of the wing, including the effect of the powered engine wakes, the total drag measured with the force balance is reduced by the computed thrust of each engine and by the drag of the five individual components of the model: wing, two engines, and two pylons. This procedure is shown in the following equations:

$$\Delta C_D = (C_D)_{\text{complete model}} - (C_D)_{\text{wing}} - (C_D)_{\text{engines}} - (C_{D,f})_{\text{pylons}}$$

where

$$(C_D)_{\text{complete model}} = (C_D)_{\text{bal}} + C_{F,n}$$

$(C_D)_{\text{bal}}$  total measured drag coefficient, based on reference wing area of  $0.936 \text{ meter}^2$ , obtained from wall-mounted strain-gage force balance

$C_{F,n}$  engine net-thrust coefficient computed as shown in appendix

$(C_D)_{wing}$	wing drag coefficient, obtained from wall-mounted strain-gage force balance during tests made with engines and pylons removed
$(C_D)_{engines} = (C_D)_{bal} + C_{F,n} - (C_D)_{pylon}$	
$(C_D)_{bal}$	measured drag coefficient obtained from engine mounted on elongated pylon
$C_{F,n}$	engine net-thrust coefficient computed as shown in appendix
$(C_D)_{pylon}$	drag coefficient of elongated pylon alone
$(C_{D,f})_{pylons}$	computed skin-friction drag coefficient of each pylon used with wing-engine-fuselage combination

#### VALIDITY OF RESULTS

The absolute force measurements made during this investigation are of little value for the following reasons: The fuselage of the test model was not attached to the balance, only the inner part of the original wing was used, and a gap drag was associated with the wing protruding through the clearance opening in the fuselage. Furthermore, because of the limitations of the instrumentation, the computed thrust values are not considered reliable as absolute values. Therefore, most of the absolute results of the investigation are not presented herein. The drag results for the basic wing-alone configuration are presented in figure 7 to indicate the compressibility drag rise characteristics of the test configuration.

The analysis presented is based on the differential values of the data referred to as "Interference Drag." The validity of these increments is considerably greater than that of the absolute results. Any systematic inaccuracies in drag measured by the force balance tend to cancel when the drag of the complete configuration is reduced by the measured drag of the wing-alone configuration. Also, the systematic errors in computing thrust tend to cancel, since the thrust of the complete configuration is added to the total balance-drag value, whereas the thrust for the engine-alone configuration is subtracted as shown in the interference-drag equation. However, even these incremental results are subject to the following qualification:

Data were not corrected for the upward inclination of the thrust vector at angles of attack greater than  $0^\circ$ . Such an inclination increases the lift and reduces the thrust measured by the balance. An analysis of the effect of such changes suggests that at angles of

attack near that for cruise, this upward inclination results in a decrease of approximately 0.0001 in the interference-drag coefficients presented herein. At the highest test angle of attack of  $4^{\circ}$ , an increase of approximately 0.0002 in the interference-drag coefficients occurs.

The results presented are also subject to random errors that possibly exist in the force-balance measurements and computed thrust. However, the results presented are considered sufficiently reliable to be indicative of the general interference phenomenon that exists for the engine-pylon-wing combination.

## RESULTS AND DISCUSSION

### Interference Drag

The aerodynamic-interference-drag coefficients obtained for the various engine positions investigated are presented in figure 8 as a function of Mach number at the cruise lift coefficient of 0.5. These data indicate that with the engines located in the most forward and lowest vertical test position relative to the wing (pylons 1 and 6), favorable interference is produced at the cruise Mach number of 0.775. The interference-drag-coefficient results for each powered-engine position tested, including the results obtained for the short- and long-duct flow-through nacelles, are presented in figure 9 as a function of lift coefficient at each test Mach number. These data indicate that at the cruise Mach number of 0.775 for each powered-engine position tested, there is generally a reduction in interference-drag coefficient with an increase in lift coefficient up to approximately the cruise lift coefficient. A similar trend is found in reference 1 wherein it was concluded that part of this favorable interference is obtained from the underwing fence action of the nacelle-pylon combination. The result of this fence action would be a reduction in wing lift vortex strength and, as a consequence, a reduction in induced drag as noted in the force results.

The effects of power, engine position, and Mach number on the overall pressure distributions on the lower surface of the wing just inboard of the wing-pylon junctures, on the pylon inboard surface, and on the engines just inboard of the pylon-engine juncture are presented in figures 10, 11, and 12, respectively.

The data obtained for the basic pylon position shown in figure 10 indicate that the greatest effect of engine wake is realized in the immediate vicinity of the engine. There is an increase in the engine surface pressures on the fan cowl inboard surfaces as a result of the engine wake flow, particularly on the inboard engine.

The loss in favorable aerodynamic interference associated with the rearward and vertical movement of the engine shown by the force data is substantiated by the pressure data shown in figure 11. The greatest effect of engine position is denoted by the change

in both the wing and pylon pressures. These data indicate a loss in pylon spanwise side force as a result of a decrease in wing and mid row pylon pressures.

An increase in Mach number (fig. 12) also causes a reduction in pressure on the wing lower surface just inboard of the pylons and on the inboard surface of the basic pylons themselves, which, in both cases, is indicative of a reduction in pylon side force and a reduction in favorable interference.

### Power Effect

The effect of power on aerodynamic interference drag can readily be seen from figure 9(a) in which  $\Delta C_D$  is presented as a function of lift coefficient for the maximum engine fan-exit pressure ratio of 1.5 and a fan-exit pressure ratio of 1.0, where the engine is operated just fast enough to overcome the internal drag of the engine. Tests at a pressure ratio of 1.0 were performed only on the pylon 1 configuration. These data show a decrease in interference drag with an increase in lift coefficient for the zero-thrust condition up to a lift coefficient of 0.5 at the cruise Mach number of 0.775. The addition of power results in a further reduction in interference drag such that favorable interference ( $-\Delta C_D$ ) is produced at the cruise Mach number. It has been proposed in reference 1 that a possible explanation for this effect of the powered-engine wake on aerodynamic interference is that the engine becomes a more effective end plate on the pylon at full-thrust conditions; thereby the engine-pylon underwing fence effectiveness is increased. It has been shown in reference 3, wherein a powered engine was mounted at the tip of an unswept symmetrical panel, that the high-energy engine wake tends to retard the development of the lift vortex normally shed from the panel, thereby increasing the panel (or pylon) efficiency.

The increase in engine-pylon side force associated with the maximum engine fan-exit pressure ratio of 1.5 compared with that for the fan-exit pressure ratio of 1.0 is shown in figure 13 by the differential pressure coefficients for the basic configuration. In this figure the difference in the engine pressure coefficients measured on the engine turbine cowl and plug outboard surface along the engine-pylon juncture and those measured along the inboard surface of the engine-pylon juncture are presented as a function of engine length in percent mean geometric chord. These data indicate that a considerably greater force develops at the engine-pylon juncture under the maximum thrust conditions.

The differential pressure data of figure 13 also indicate that there is an inward side force in the region of the engine-pylon juncture at the lower angles of attack. This adverse side force is possibly the result of the  $1^{\circ}$  engine toe-in set in both the inboard and the outboard engines. As the angle of attack is increased, the lift-induced spanwise flow on the wing causes a reversal of engine side force and therefore an increase in favorable interference.

The pylon differential pressure distributions shown in figure 14, obtained from pressures measured streamwise along the middle of the pylon and on the pylon just below the wing, are presented as a function of longitudinal distance in percent mean geometric chord for the engine fan-exit pressure ratios of 1.5 and 1.0. These data indicate that there is an outward force on the pylons which increases with angle of attack. This force increase is the result of the retarding action of the engine-pylon combinations to the underwing spanwise flow and is similar to that found at the engine-pylon juncture. The slightly greater pylon side force for the power-on case ( $p_{t,e}/p_{t,\infty} = 1.5$ ) than that for the case in which  $p_{t,e}/p_{t,\infty} = 1.0$  indicates only a slight effect of power in this region. Also note that more side force is produced by the inboard engine-pylons combination.

#### Engine-Wake Simulation

During one phase of the present investigation, an attempt was made to simulate the engine on the model by replacing each engine with a short-duct flow-through nacelle. (See fig. 5(b).) In an attempt to simulate the effect of the wake of the powered engines on interference drag, the flow-through-nacelle fan cowl was extended to approximately the turbine exit location to simulate the boundary of the wake. (See fig. 5(b).) The interference-drag results for the short- and long-duct flow-through nacelles and for the powered engines operated at fan-exit pressure ratios of 1.0 and 1.5 are presented as a function of Mach number in a summary plot for a lift coefficient of 0.5. (See fig. 15.) These data indicate that at the cruise Mach number of 0.775 the interference-drag results for the short-duct nacelle configuration are similar to those of the powered-engine configuration at  $p_{t,e}/p_{t,\infty} = 1.0$ . The drag results for the long-duct wake-simulating nacelle configuration approach those for the powered engines at the maximum exit pressure ratio, so that the difference between the short-duct nacelle and the powered engine was reduced by approximately one-half.

#### SUMMARY OF RESULTS

An experimental investigation to determine the effect of engine position and fan-jet wake on the aerodynamic interference of a high-wing four-engine logistics transport airplane indicates the following results:

1. Favorable aerodynamic interference drag was produced at the design cruise lift coefficient and Mach number by properly positioning the engines of the airplane configuration used in this investigation. The largest favorable interference-drag values were obtained with the engines in the most forward and lowest vertical position relative to the wing.

2. Engine wake increases the engine-pylon loading in the spanwise direction, particularly in the vicinity of the engine-pylon juncture as a result of an increase in the fence effectiveness of the combination. This effect on aerodynamic interference drag is such that favorable interference is produced for the power-on case compared with the unfavorable interference associated with the power-off case with the engine in the most favorable position at cruise conditions.

3. An increase in Mach number above the design cruise Mach number of 0.775 for this particular airplane configuration has an adverse influence on the aerodynamic interference drag.

4. An extension of the fan cowl of a short-duct flow-through nacelle to simulate the effect of the engine wake on interference drag reduces the difference in interference drag between the short-duct flow-through nacelle and the powered engine by approximately one-half.

Langley Research Center,  
National Aeronautics and Space Administration,  
Hampton, Va., September 15, 1970.

## APPENDIX

### COMPUTATIONS

#### Forces

The forces measured with the force balance are reduced to lift and drag coefficients by use of the semispan wing area of 0.936 meter<sup>2</sup>.

#### Thrust

The net thrust of the model engines, determined from the initial free-stream conditions and internal total and static pressures at the fan and primary inlets and exits including the scrubbing drag resulting from the fan and primary exit flows, is

$$F_n = F_{g,f} - D_r + F_{g,p} - D_s$$

Fan gross thrust. - The fan gross thrust is computed on the basis of the average of the individual products of the fan-inlet mass-flow rate and the fan-exit velocity plus the fan-exit pressure force:

$$F_{g,f} = (\dot{m}_i V_e)_{av} + [(p_e)_{av} + p_\infty] A_e$$

The mass-flow rate and fan-exit velocity are determined from each total pressure measured at each rake probe and the static-pressure value that exists at the total-pressure probe. The static-pressure value is determined by assuming that a linear variation of the static pressure exists between two static orifices, one just inside the fan cowl exit and one on the turbine surface located circumferentially at each total-pressure rake position. The exit mass-flow rate normally used to compute the gross thrust has been replaced by the inlet mass-flow rate which has been adjusted by the constant obtained from the previously mentioned inlet calibration and is therefore assumed to be more reliable. This mass-flow rate is obtained by computing the mass-flow rate at each total-pressure probe and summing them as follows:

$$\dot{m}_i = K \sum (\rho V A)_j$$

where  $j$  is at each inlet total-pressure probe.

The density at each pressure probe is computed by use of the thermal equation of state:

$$\rho = \frac{p}{RT_{st}}$$

## APPENDIX – Continued

The inlet static pressure was measured as described previously, whereas the local static temperature was determined from the measured stream total temperature and the local inlet Mach number as follows:

$$T_{st} = \frac{T_{t,\infty}}{1 + \frac{\gamma - 1}{2} M^2}$$

The inlet Mach number is computed in the conventional manner for each inlet total and static pressure measured.

The local fan-inlet velocity is computed as follows:

$$V = M\sqrt{\gamma RT_{st}}$$

The fan-exit velocity, required in computing fan gross thrust, is determined in a manner similar to that used for determining the inlet velocity based on the total-pressure and static-pressure measurements at the fan exit.

$$V_e = M_e\sqrt{\gamma RT_{st,e}} \left(\frac{\dot{m}_i}{\dot{m}_e}\right)^{0.6}$$

It is necessary to correct the fan-exit velocity for the inaccuracy encountered in the fan-exit stagnation-pressure measurements made in the exit-duct boundary layer. The fan-exit mass-flow rate is replaced by the calibrated fan-inlet mass-flow rate, thus, the effect of the instrumentation error by this substitution is eliminated, as stated previously. The fan-exit velocity is in error by the same amount as the ratio of the inlet to the exit mass-flow rate ( $\dot{m}_i/\dot{m}_e$ ), which is due to the displacement thickness. To account for the error in momentum, this ratio is adjusted by the ratio of momentum to displacement thickness, which is 0.6 at a Mach number of 0.80 (ref. 4). This correction is applied as  $(\dot{m}_i/\dot{m}_e)^{0.6}$ , which gives 0.6 of the percent error found between the inlet and exit mass-flow rates.

Ram drag. - The ram drag is the initial momentum of the air entering the fan inlet and is the product of the mass-flow rate determined from inlet measurements as previously shown and the stream velocity:

$$D_r = \dot{m}_i V_\infty$$

## APPENDIX – Concluded

Primary thrust. - The primary gross thrust is obtained in a manner similar to that used to determine fan gross thrust:

$$F_{g,p} = (\dot{m}_{p,e} V_{p,e})_{av} + [(p_{p,e})_{av} - p_{\infty}] A_{p,e}$$

The primary inlet mass-flow rate was determined by a flowmeter located in the nitrogen line.

The primary exit velocity used in the computation of thrust was also corrected by use of the ratio of the turbine inlet mass-flow rate to the exit mass-flow rate to the 0.6 power.

Scrubbing drag. - A correction is applied to the thrust computations of the present test for the scrubbing drag. This skin-friction drag is the sum of the scrubbing drag on the fan cowl, on the turbine cowl, and on the primary exit plug. Each component is obtained from the following equation:

$$D_s = C_f(A)_{wet} q$$

The scrubbing drag is computed by using the dynamic pressure and Reynolds number based on local conditions over the fan cowl, fan-exit conditions over the turbine cowl, and primary exit conditions over the plug. The friction coefficient is obtained from the Sommer and Short T' method as given in reference 5.

Thrust coefficient. - The thrust is reduced to coefficient form by using the free-stream dynamic pressure and the wing reference area in the following manner:

$$C_{F,n} = \frac{F_n}{q_{\infty} S}$$

These thrust coefficients for the complete airplane configuration and for the engine alone are used in the determination of the interference drag.

## REFERENCES

1. Patterson, James C., Jr.: A Wind-Tunnel Investigation of Jet-Wake Effect of a High-Bypass Engine on Wing-Nacelle Interference Drag of a Subsonic Transport. NASA TN D-4693, 1968.
2. Wright, Ray H.; Ritchie, Virgil S.; and Pearson, Albin O.: Characteristics of the Langley 8-Foot Transonic Tunnel With Slotted Test Section. NACA Rep. 1389, 1958. (Supersedes NACA RM L51H10 by Wright and Ritchie and RM L51K14 by Ritchie and Pearson.)
3. Patterson, James C., Jr.; and Flechner, Stuart G.: An Exploratory Wind-Tunnel Investigation of the Wake Effect of a Panel Tip-Mounted Fan-Jet Engine on the Lift-Induced Vortex. NASA TN D-5729, 1970.
4. Shapiro, Ascher H.: The Dynamics and Thermodynamics of Compressible Fluid Flow. Vol. II, Ronald Press Co., c.1954, p. 1093.
5. Sommer, Simon C.; and Short, Barbara J.: Free-Flight Measurements of Turbulent-Boundary-Layer Skin Friction in the Presence of Severe Aerodynamic Heating at Mach Numbers From 2.8 to 7.0. NACA TN 3391, 1955.

TABLE I.- MODEL COORDINATES

(a) Coordinates for wing

[Stations and ordinates in percent wing mean geometric chord]

0-m station; 0° incidence				0.695-m station				0.82-m station; -1.50° incidence				1.081-m station				1.904-m station; -3.50° incidence			
Upper surface		Lower surface		Upper surface		Lower surface		Upper surface		Lower surface		Upper surface		Lower surface		Upper surface		Lower surface	
Station	Ordinate	Station	Ordinate	Station	Ordinate	Station	Ordinate	Station	Ordinate	Station	Ordinate	Station	Ordinate	Station	Ordinate	Station	Ordinate	Station	Ordinate
0	0	0	0	0	0	0	0	0	0	0	0	0	0	0	0	0	0	0	0
-.03	.83	.40	-.73	-.03	.58	.28	-.50	-.03	.53	.25	-.46	-.03	.49	.24	-.43	-.06	.37	.18	-.33
.07	1.20	.66	-1.00	.05	.83	.45	-.69	.04	.76	.41	-.63	.02	.70	.38	-.59	-.04	.53	.29	-.44
.21	1.49	.90	-1.19	.14	1.03	.61	-.82	.13	.92	.56	-.75	.09	.87	.51	-.70	-.00	.64	.38	-.52
.36	1.75	1.11	-1.35	.24	1.20	.76	-.93	.22	1.10	.70	-.85	.17	1.01	.64	-.78	.04	.75	.46	-.58
.52	1.97	1.32	-1.49	.35	1.35	.90	-1.02	.32	1.23	.83	-.93	.26	1.14	.76	-.86	.09	.83	.53	-.62
.69	2.18	1.52	-1.61	.46	1.48	1.04	-1.10	.42	1.36	.95	-1.01	.35	1.25	.87	-.92	.14	.91	.61	-.67
1.04	2.54	1.91	-1.82	.69	1.73	1.30	-1.23	.63	1.58	1.19	-1.13	.54	1.45	1.09	-1.03	.25	1.06	.75	-.73
1.41	2.86	2.27	-2.01	.94	1.94	1.56	-1.35	.85	1.77	1.43	-1.23	.74	1.63	1.29	-1.12	.36	1.18	.87	-.79
2.38	3.54	3.14	-2.40	1.58	2.39	2.16	-1.59	1.43	2.18	1.99	-1.44	1.25	2.00	1.79	-1.31	.68	1.43	1.18	-.88
3.39	4.08	3.98	-2.75	2.24	2.75	2.75	-1.79	2.03	2.51	2.53	-1.62	1.79	2.30	2.28	-1.46	1.01	1.62	1.47	-.96
7.40	5.48	7.34	-3.92	4.88	3.71	5.10	-2.41	4.43	3.39	4.70	-2.14	3.93	3.08	4.20	-1.90	2.34	2.11	2.61	-1.13
11.1	6.35	11.0	-4.88	7.38	4.32	7.59	-2.87	6.72	3.96	6.98	-2.52	5.96	3.58	6.22	-2.20	3.59	2.39	3.85	-1.22
14.8	7.04	14.7	-5.65	9.88	4.81	10.1	-3.22	9.00	4.41	9.26	-2.79	7.26	3.97	8.25	-2.42	4.83	2.61	5.09	-1.27
22.2	8.09	22.1	-6.84	14.9	5.54	15.1	-3.71	13.6	5.09	13.8	-3.16	12.1	4.57	12.3	-2.71	7.33	2.95	7.54	-1.32
29.5	8.86	29.4	-7.73	19.9	6.08	20.1	-4.05	18.1	5.58	18.4	-3.39	16.1	5.01	16.4	-2.91	9.84	3.21	9.98	-1.38
36.9	9.43	36.8	-8.37	24.9	6.48	25.0	-4.28	22.7	5.96	22.9	-3.55	20.2	5.34	20.4	-3.04	12.4	3.40	12.4	-1.47
44.2	9.84	44.2	-8.82	29.9	6.77	30.0	-4.42	27.3	6.23	27.5	-3.64	24.3	5.57	24.4	-3.14	14.9	3.53	14.8	-1.59
51.6	10.1	51.6	-9.08	34.9	6.96	35.0	-4.49	31.9	6.40	32.0	-3.67	28.4	5.72	28.5	-3.20	17.4	3.57	17.3	-1.72
58.9	10.2	59.0	-9.14	39.9	7.05	40.0	-4.48	36.5	6.49	36.6	-3.65	32.5	5.78	32.5	-3.20	19.9	3.55	17.8	-1.80
66.2	10.2	66.4	-9.01	44.9	7.05	44.9	-4.40	41.1	6.50	41.1	-3.58	36.5	5.77	36.6	-3.15	22.4	3.47	22.3	-1.81
73.6	9.98	73.8	-8.69	49.9	6.96	49.9	-4.24	45.6	6.42	45.7	-3.45	40.6	5.67	40.6	-3.04	24.8	3.33	24.7	-1.76
80.9	9.68	81.2	-8.20	54.9	6.77	54.9	-4.01	50.2	6.25	50.2	-3.26	44.7	5.49	44.7	-2.87	27.3	3.13	27.2	-1.65
88.3	9.25	88.6	-7.55	59.9	6.49	59.9	-3.71	54.8	6.00	54.8	-3.03	48.8	5.24	48.7	-2.65	29.8	2.89	29.7	-1.49
95.7	8.72	95.9	-6.74	64.9	6.13	64.9	-3.34	59.4	5.66	59.3	-2.73	52.8	4.92	52.8	-2.39	32.3	2.60	32.2	-1.30
103.1	8.05	103.2	-5.83	69.9	5.87	69.8	-2.90	64.0	5.25	63.9	-2.38	56.9	4.53	56.8	-2.07	34.8	2.27	34.6	-1.10
110.5	7.24	110.6	-4.84	74.9	5.10	74.8	-2.43	68.6	4.72	68.4	-2.01	61.0	4.05	60.9	-1.73	37.2	1.93	37.1	-.89
117.9	6.27	117.9	-3.79	79.9	4.40	79.7	-1.95	73.2	4.06	72.9	-1.63	65.1	3.46	64.9	-1.39	39.7	1.58	39.6	-.65
125.3	5.14	125.2	-2.72	85.0	3.55	84.7	-1.47	77.7	3.27	77.5	-1.25	69.1	2.78	68.9	-1.05	42.1	1.23	42.1	-.43
132.7	3.78	132.5	-1.72	89.9	2.56	89.7	-.99	82.3	2.34	82.1	-.87	73.2	1.99	73.0	-.71	44.6	.87	44.6	-.23
140.1	2.15	139.9	-.85	94.9	1.42	94.7	-.54	86.8	1.29	86.7	-.48	77.2	1.09	77.1	-.39	47.1	.48	47.1	-.10
147.4	.19	147.3	-.19	99.8	.11	99.8	-.11	91.3	.10	91.3	-.10	81.2	.09	81.2	-.09	49.6	.05	49.6	-.05

TABLE I.- MODEL COORDINATES - Continued

(b) Coordinates for pylons

[Stations and ordinates in percent wing mean geometric chord]

At wing (a)	Station						Ordinate
	All pylons	At engine					
		Pylon 1 (b)	Pylon 2	Pylon 3	Pylon 4	Pylon 5	
0	0	0	0	0	0	0	0
.10	.10	.10	.10	.10	.10	.10	.40
.21	.21	.22	.21	.21	.21	.21	.57
.31	.31	.36	.31	.31	.31	.31	.71
.41	.41	.52	.41	.41	.41	.41	.85
.52	.52	.62	.52	.52	.52	.52	.93
.62	.62	.80	.62	.62	.62	.62	1.03
.83	.83	1.08	.83	.83	.83	.83	1.18
1.04	1.04	1.36	1.04	1.04	1.04	1.04	1.31
1.56	1.56	2.07	1.56	1.56	1.56	1.56	1.58
2.07	2.07	2.56	2.07	2.07	2.07	2.07	1.81
4.15	4.15	5.90	4.15	4.15	4.15	4.15	2.34
6.22	6.22	8.58	6.22	6.22	6.22	6.22	2.68
8.30	8.30	12.1	8.30	8.30	8.30	8.30	2.93
12.5	12.5	17.8	12.5	12.5	12.5	12.5	3.25
16.6	16.6	22.4	16.6	16.6	16.6	16.6	3.39
20.7	20.7	29.0	20.7	20.7	20.7	20.7	3.51
24.9	24.9	33.2	24.9	24.9	24.9	24.9	3.53
33.2	61.7	61.7	48.6	57.0	52.4	39.5	3.53
37.3	65.8	65.8	52.7	61.1	56.6	43.6	3.51
41.5	70.0	70.0	56.9	65.3	60.7	47.8	3.44
45.6	74.1	74.1	61.0	69.4	64.9	51.9	3.34
49.8	78.3	78.3	65.2	73.6	69.0	56.1	3.18
53.9	82.4	82.4	69.3	77.7	73.2	60.2	2.98
58.1	86.6	86.6	73.4	81.9	77.3	64.4	2.73
62.2	90.7	90.7	77.6	86.0	81.5	68.5	2.43
66.4	94.9	94.9	81.7	90.2	85.6	72.7	2.07
70.5	99.0	99.0	85.9	94.3	89.8	76.8	1.66
74.7	103.2	103.2	90.0	98.5	93.9	81.0	1.19
78.8	107.3	107.3	94.2	102.6	98.1	85.1	.66
83.0	111.5	111.5	98.3	106.8	102.2	89.3	.07

<sup>a</sup>Also at the nacelle for the pylon for the long-duct flow-through nacelle.

<sup>b</sup>Also at the nacelle for the pylon for the short-duct flow-through nacelle.

TABLE I.- MODEL COORDINATES - Continued

(c) Coordinates for fan-jet engine

[Stations and radii in percent wing mean geometric chord]

Fan cowl		Turbine cowl		Plug	
Station	Radius	Station	Radius	Station	Radius
0	24.2	34.3	18.2	70.8	8.18
.33	24.9	38.7	17.9	73.5	7.75
1.37	25.6	44.2	17.3	76.8	6.85
3.07	26.3	49.3	16.7	79.6	5.77
5.48	27.0	53.7	16.0	82.1	4.49
10.6	27.7	58.1	15.4	85.2	2.60
17.2	27.7	61.7	14.7	86.5	0
26.1	27.4	65.3	13.9		
30.2	26.8	69.0	13.9		
32.6	26.2	70.8	12.7		
34.3	25.9				

(d) Coordinates for short-duct flow-through nacelle

[Stations and radii in percent wing mean geometric chord]

Station	Inside contour	Outside contour	Station	Inside contour	Outside contour
	Radius	Radius		Radius	Radius
	Fan cowl			Turbine cowl	
0	12.1	12.1	28.9	7.09	7.09
.12	11.7	12.2	29.0	6.67	7.47
.24	11.6	12.4	29.2	6.57	7.64
.47	11.5	12.5	29.4	6.43	7.85
.95	11.4	12.7	29.9	6.26	8.11
1.42	11.3	12.9	30.3		8.42
1.89	11.2	13.0	30.8		8.63
2.36	11.2	13.0	31.3		8.75
4.25	11.2	13.4	32.7		9.03
6.14	11.4	13.6	34.1		9.12
8.03	11.5	13.8	36.5		9.01
9.93	11.6	13.9	41.2		8.84
11.8	11.7	13.9	45.9		8.49
16.5	12.0	13.9	50.7		8.23
21.3	12.3	13.9	55.4		7.85
26.0	12.6	13.7	60.1		7.47
28.4	12.7	13.6	64.9		7.02
30.7	12.9	13.4	69.6		6.45
31.7	13.0	13.3	70.0		6.38
32.6	13.0	13.2	70.8	6.26	6.35
33.6	12.9	13.0			
34.3	12.8	12.9			

TABLE I.- MODEL COORDINATES - Concluded  
(e) Coordinates for long-duct flow-through nacelle

[Stations and radii in percent wing mean geometric chord]

Inside contour		Outside contour	
Station	Radius	Station	Radius
0	12.5	0	12.5
.24	12.4	.24	12.8
.47	12.3	.47	13.0
.71	12.2	.71	13.0
1.42	11.9	1.42	13.2
2.13	11.7	2.13	13.3
2.84	11.6	2.84	13.4
3.09	11.5	3.09	13.5
62.3	11.5	3.78	13.5
		4.73	13.7
		5.67	13.7
		6.62	13.7
		7.56	13.8
		8.34	13.8
		20.7	13.8
		20.8	13.7
		22.7	13.7
		24.6	13.7
		26.5	13.5
		28.4	13.4
		30.3	13.3
		31.2	13.1
		32.4	12.9
		34.0	13.0
		35.5	12.9
		40.2	12.7
		44.9	12.7
		49.6	12.5
		53.9	12.2
		58.1	12.0
		62.3	11.6

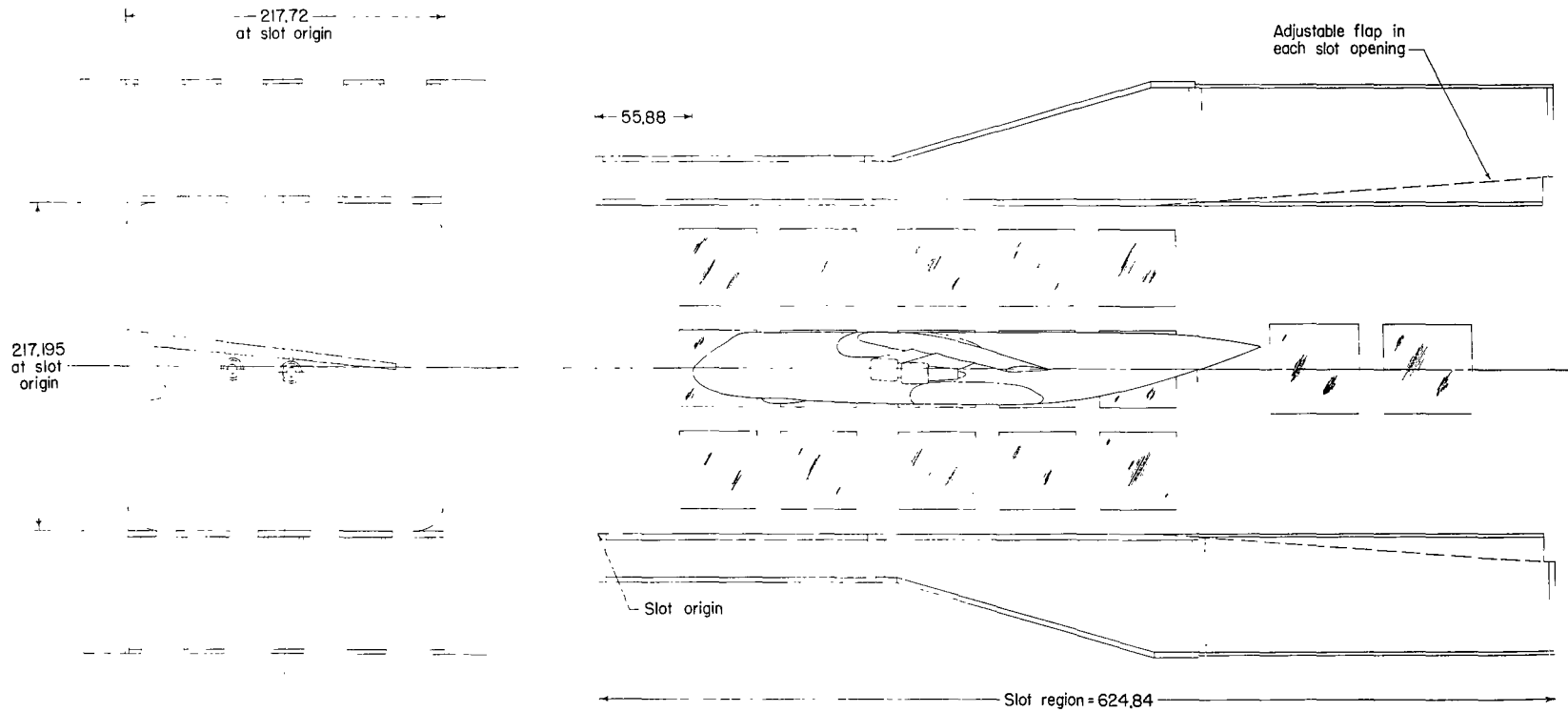
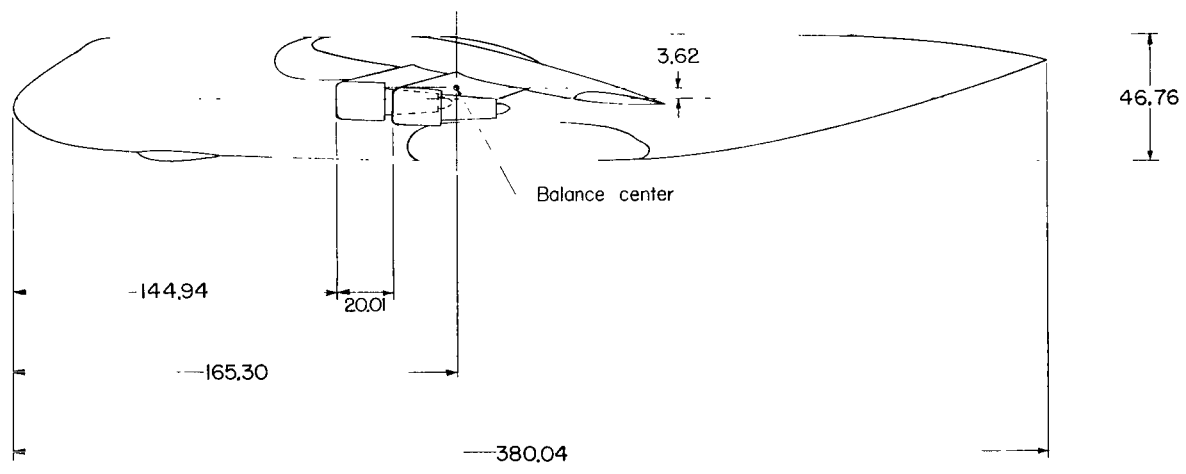
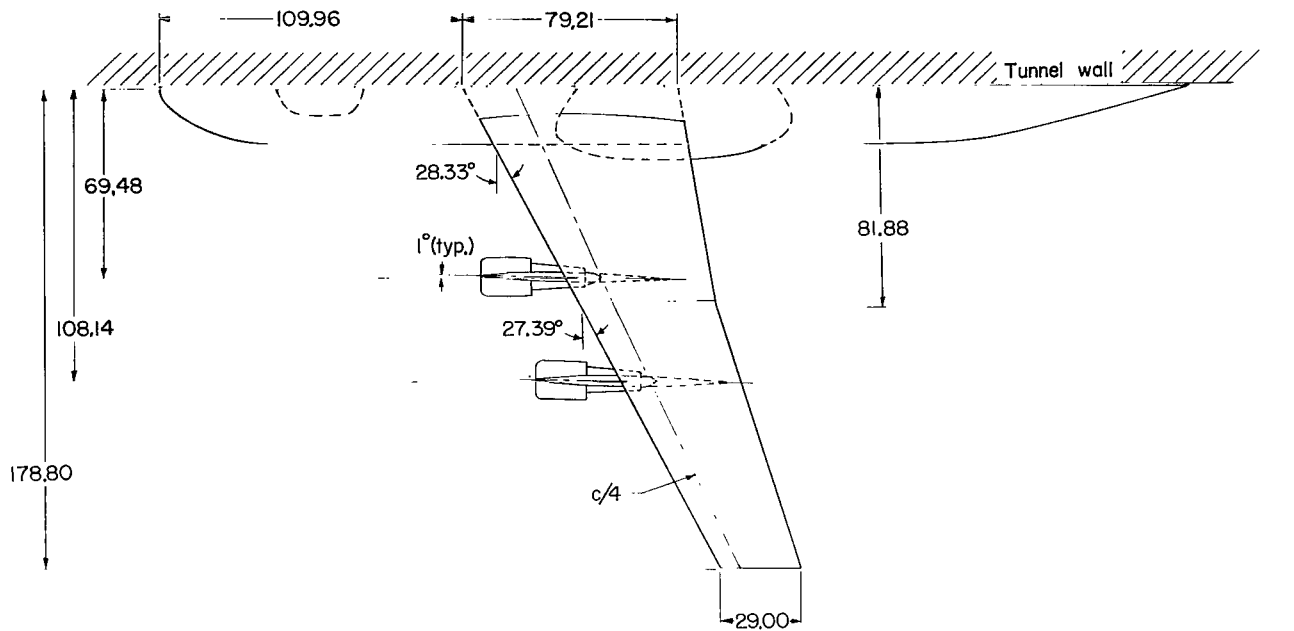
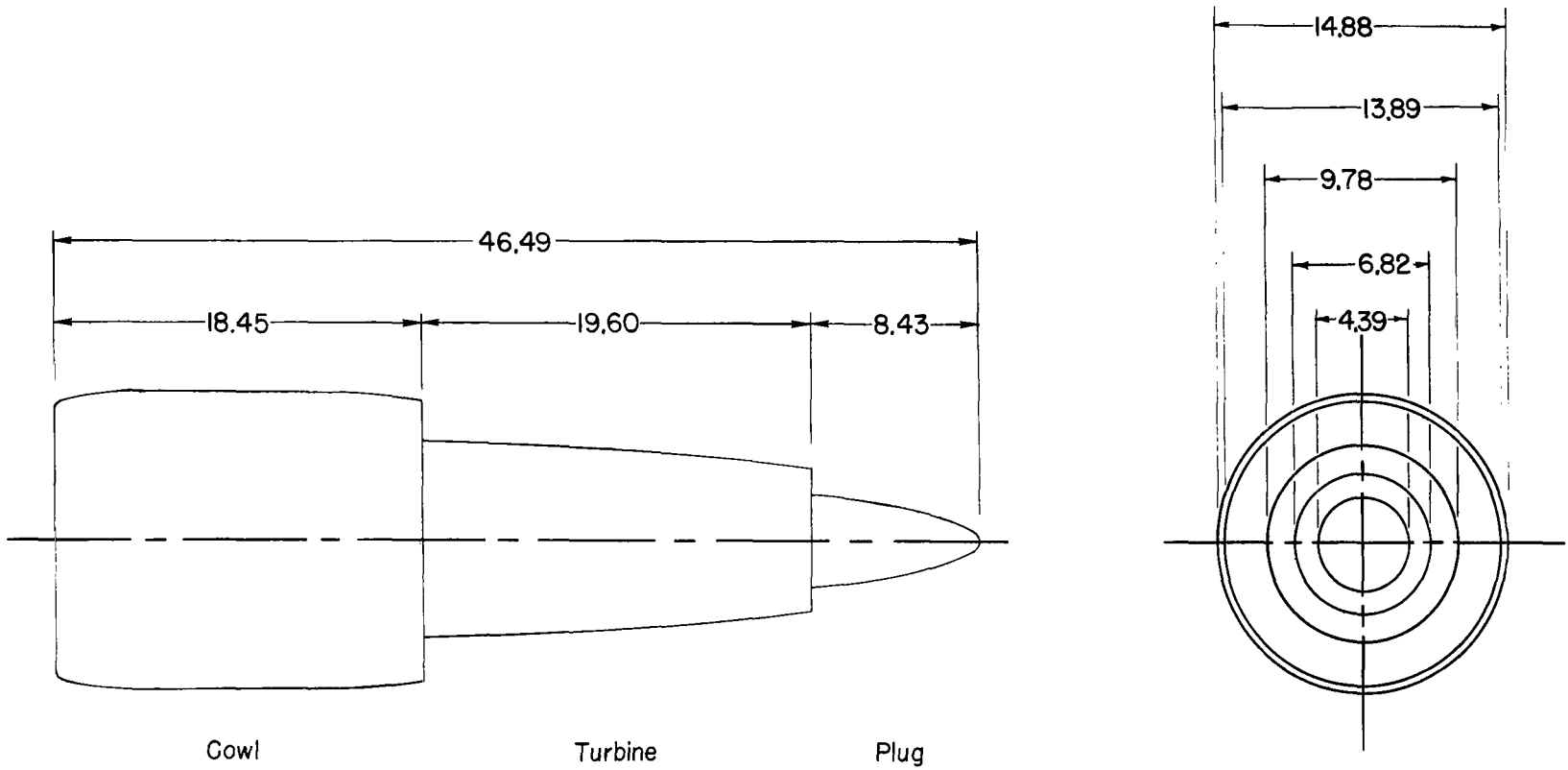


Figure 1.- Details of test section and location of model in Langley 8-foot transonic pressure tunnel. All dimensions are in centimeters.



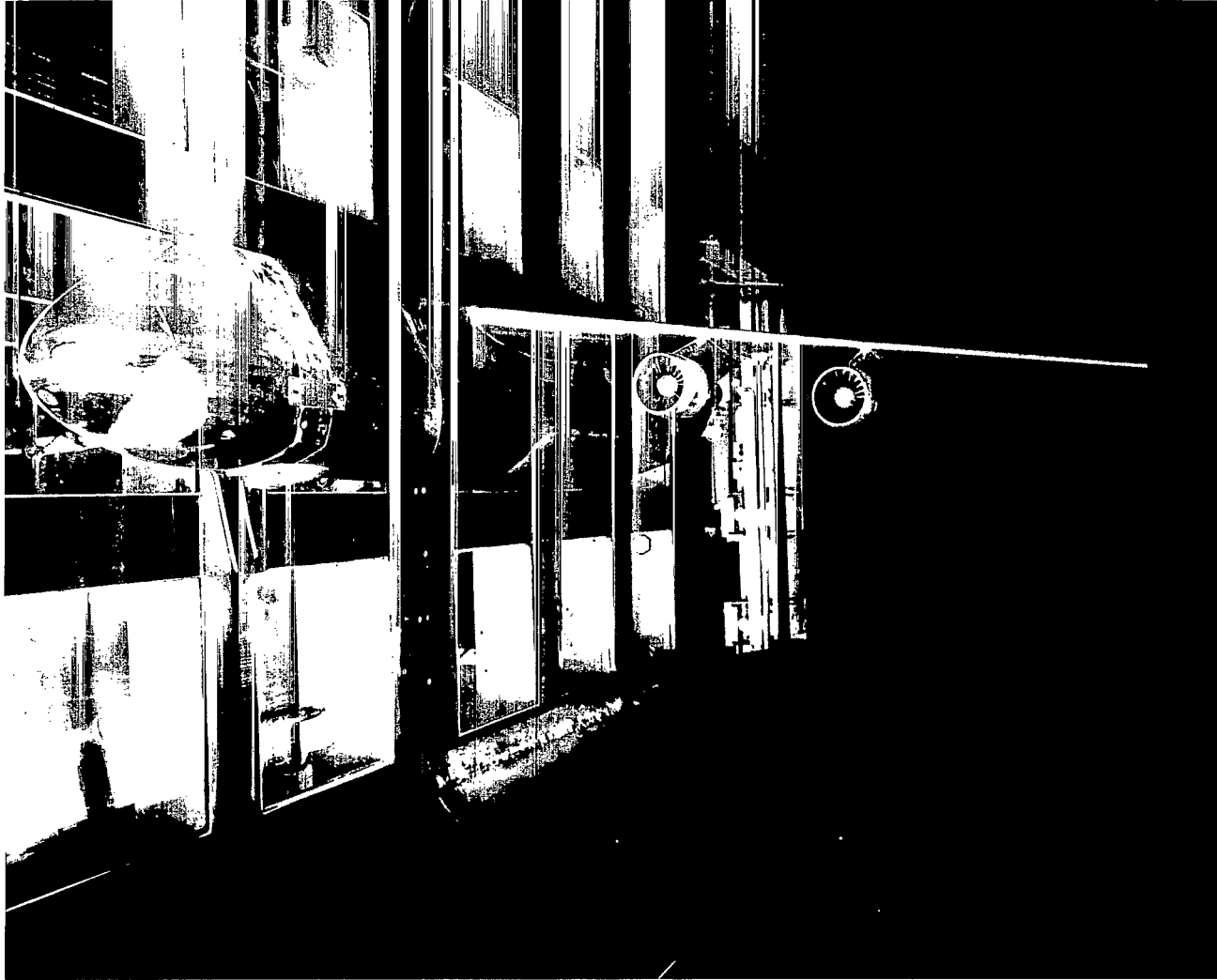
(a) Details of test model.

Figure 2.- Drawing of the semispan transport model. All dimensions are in centimeters.



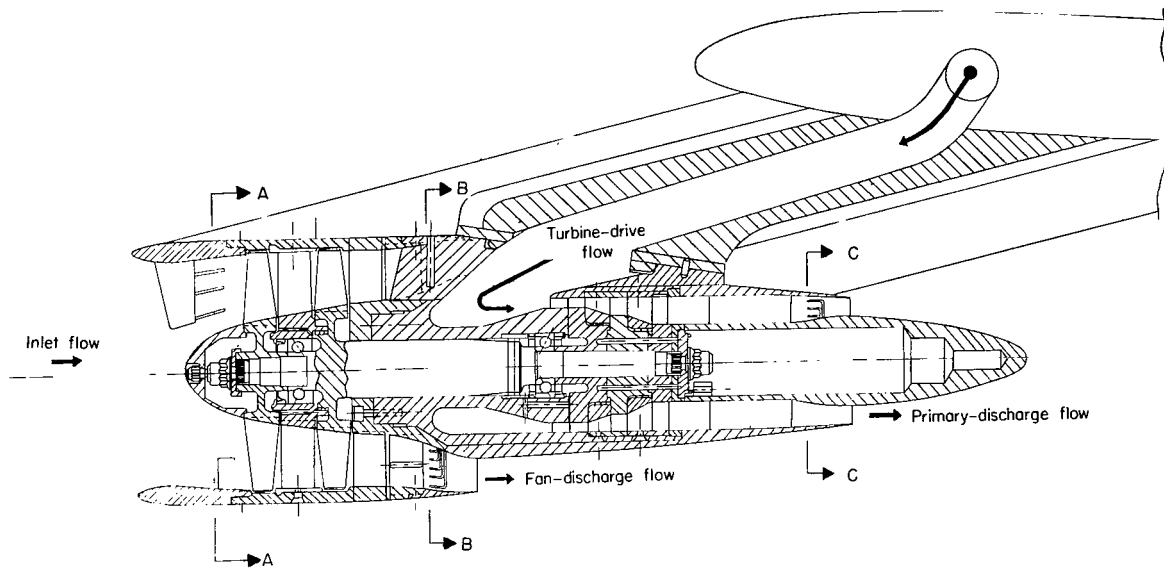
(b) Details of powered model engine nacelle.

Figure 2.- Concluded.



L-66-1766

Figure 3.- Photograph of semispan model mounted on wall of the Langley  
8-foot transonic pressure tunnel.



Total-pressure rakes (unless otherwise stated)

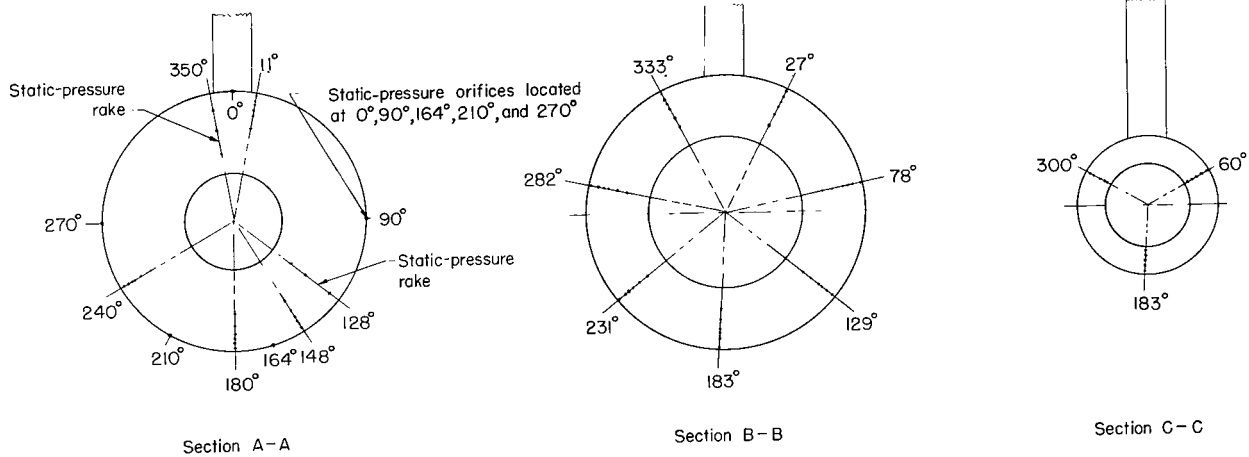
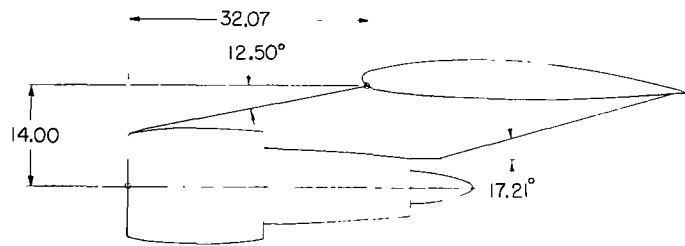
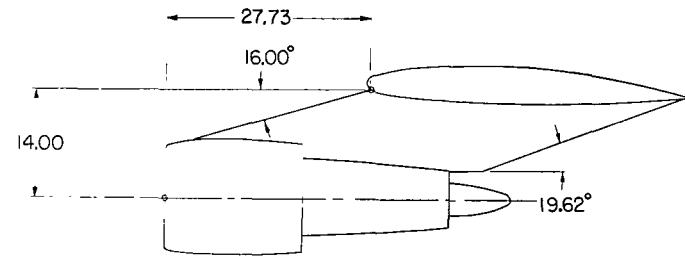


Figure 4.- Cross-sectional view of model fan-jet engine.



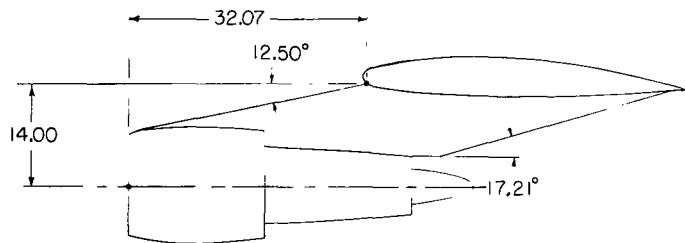
Pylon 1

Basic



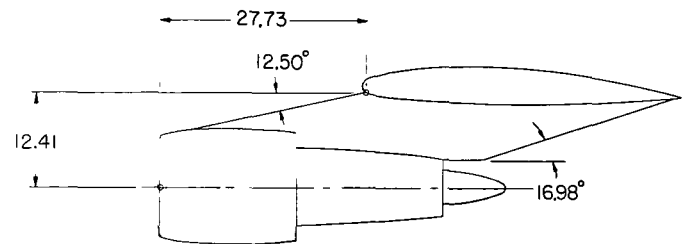
Pylon 3

Longitudinal variation



Pylon 2

Thickness variation

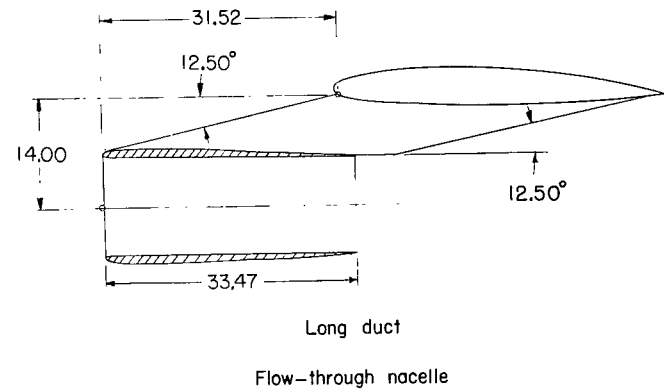
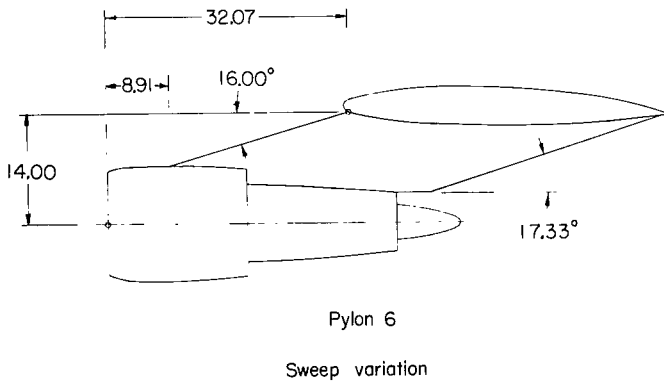
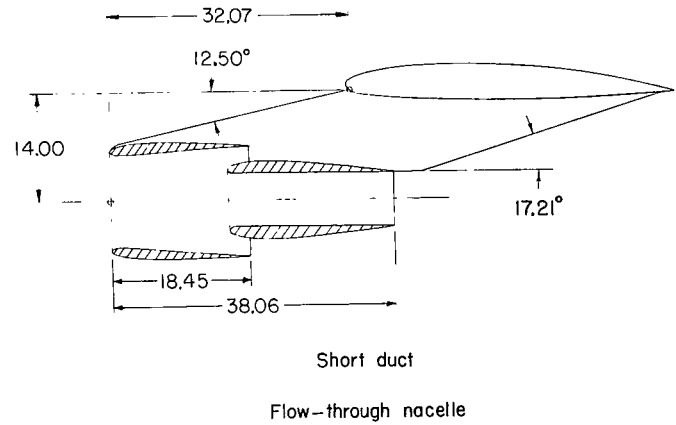
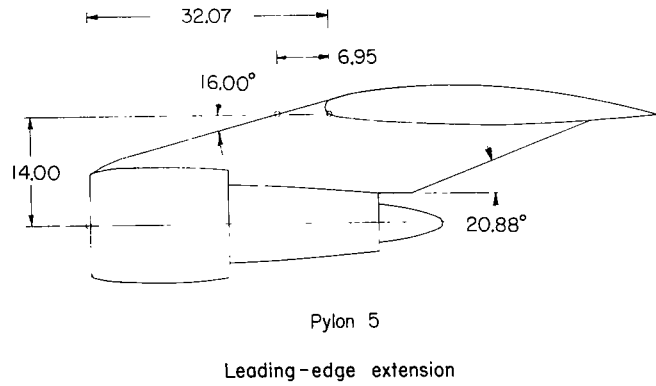


Pylon 4

Longitudinal and vertical variation

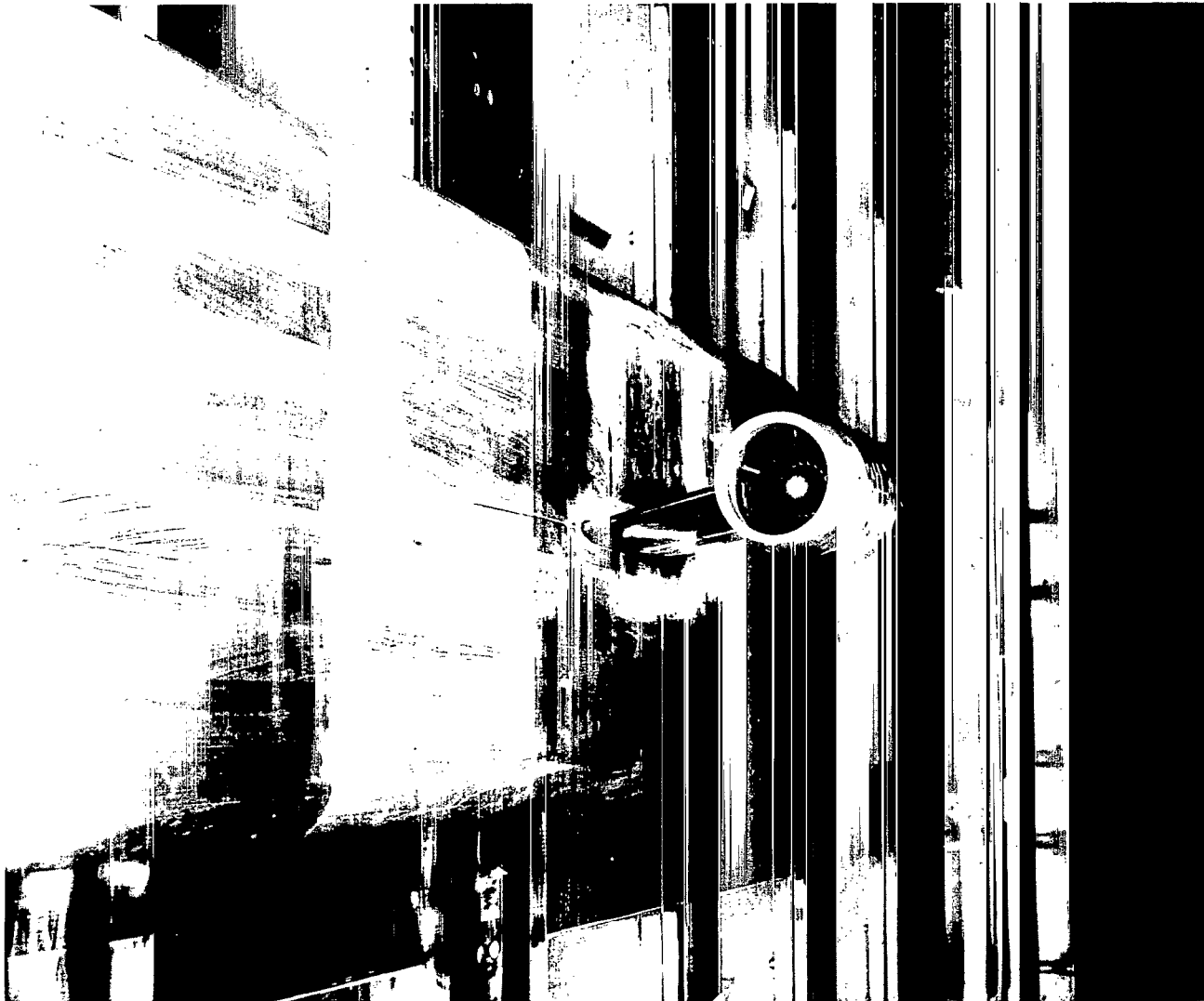
(a) Powered-engine locations.

Figure 5.- Details of engine locations. Juncture of pylon leading edge and wing is at 1.4 percent local chord. All dimensions are in centimeters.



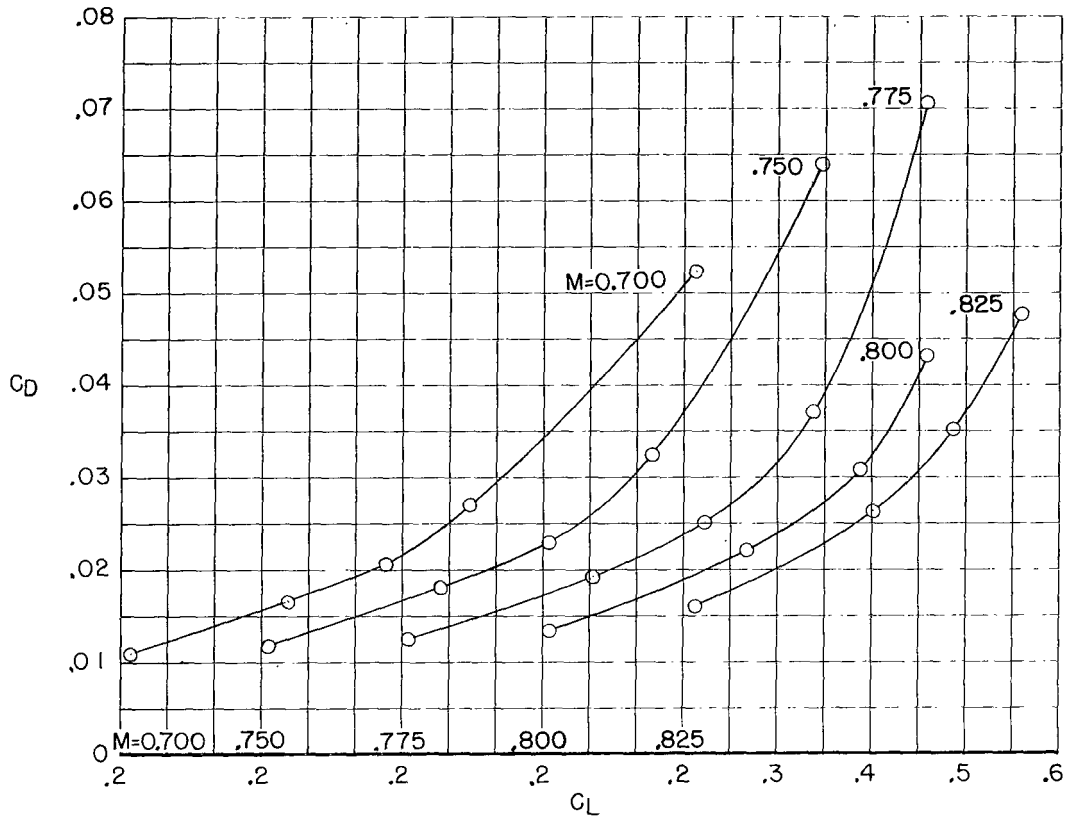
(b) Engine and flow-through-nacelle locations.

Figure 5.- Concluded.

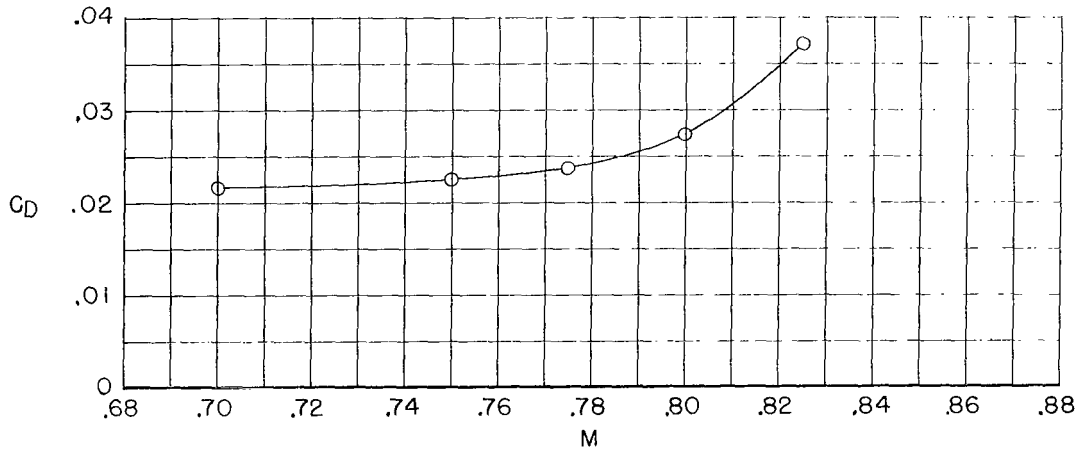


I-65-4643

Figure 6.- Photograph of model engine and elongated pylon wall-mounted in  
Langley 8-foot transonic pressure tunnel.



(a) Variation of drag coefficient with lift coefficient for various Mach numbers.



(b) Variation of drag coefficient with Mach number for lift coefficient of 0.5.

Figure 7.- Drag characteristics of basic wing-alone configuration.

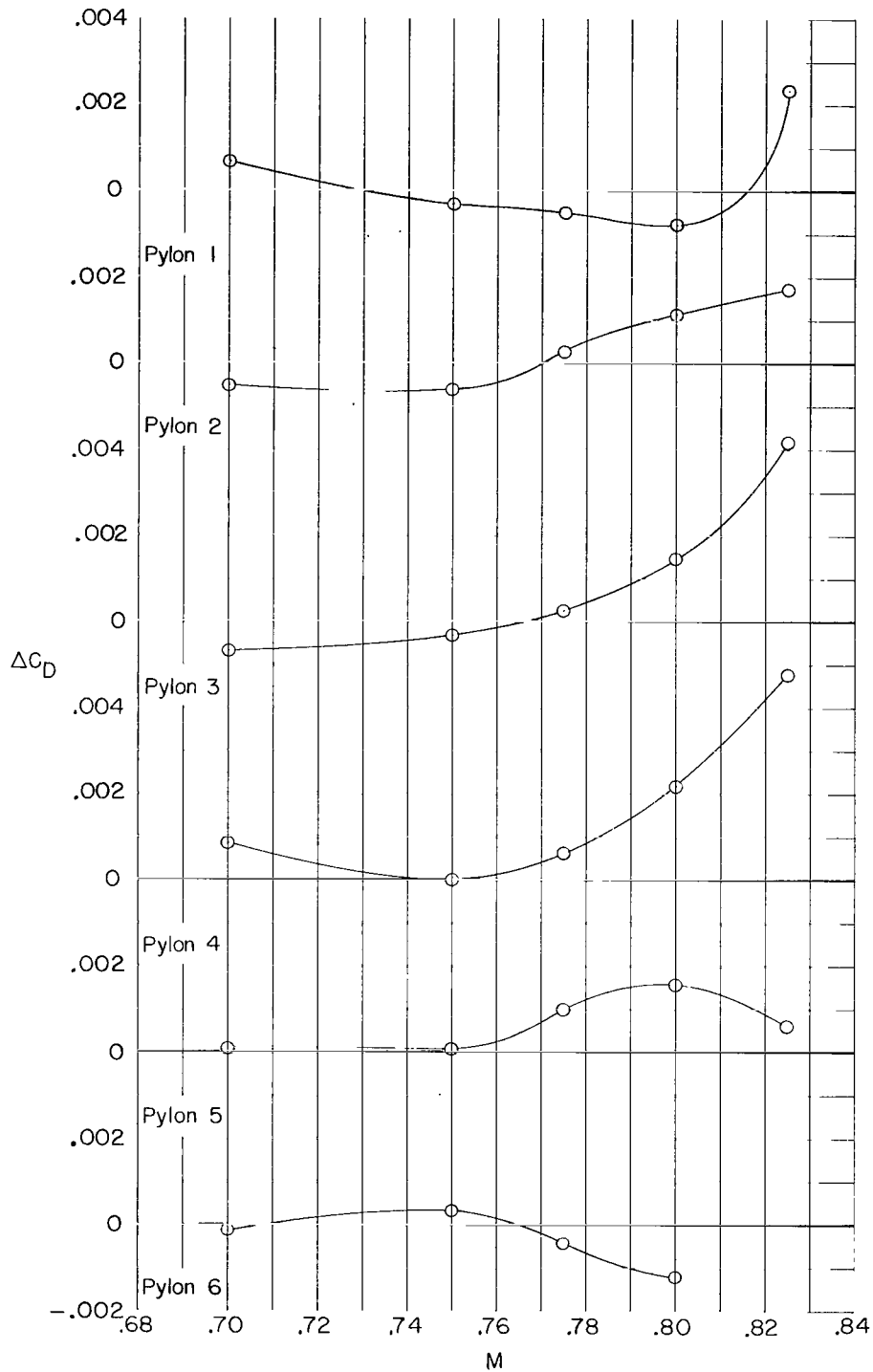
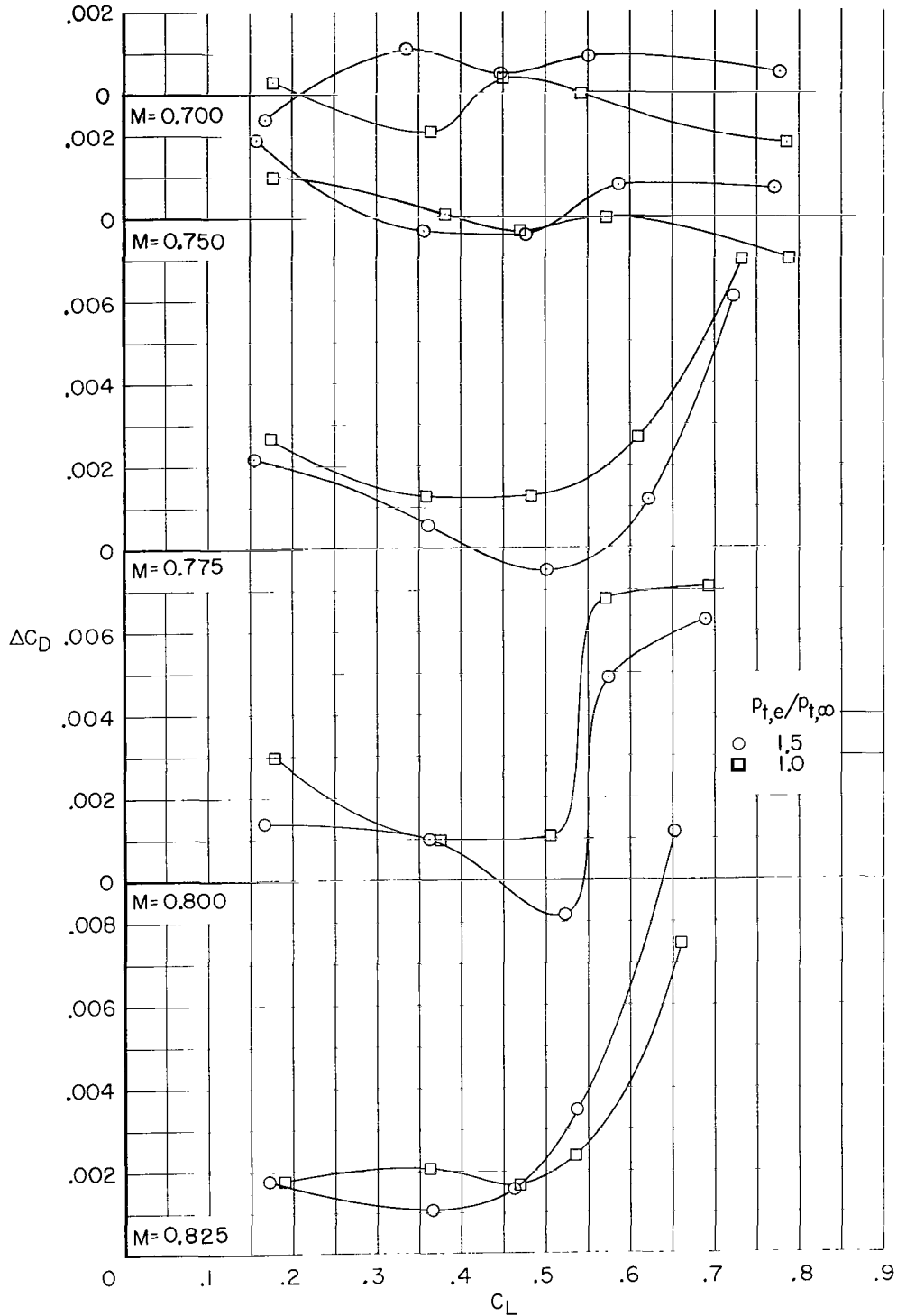
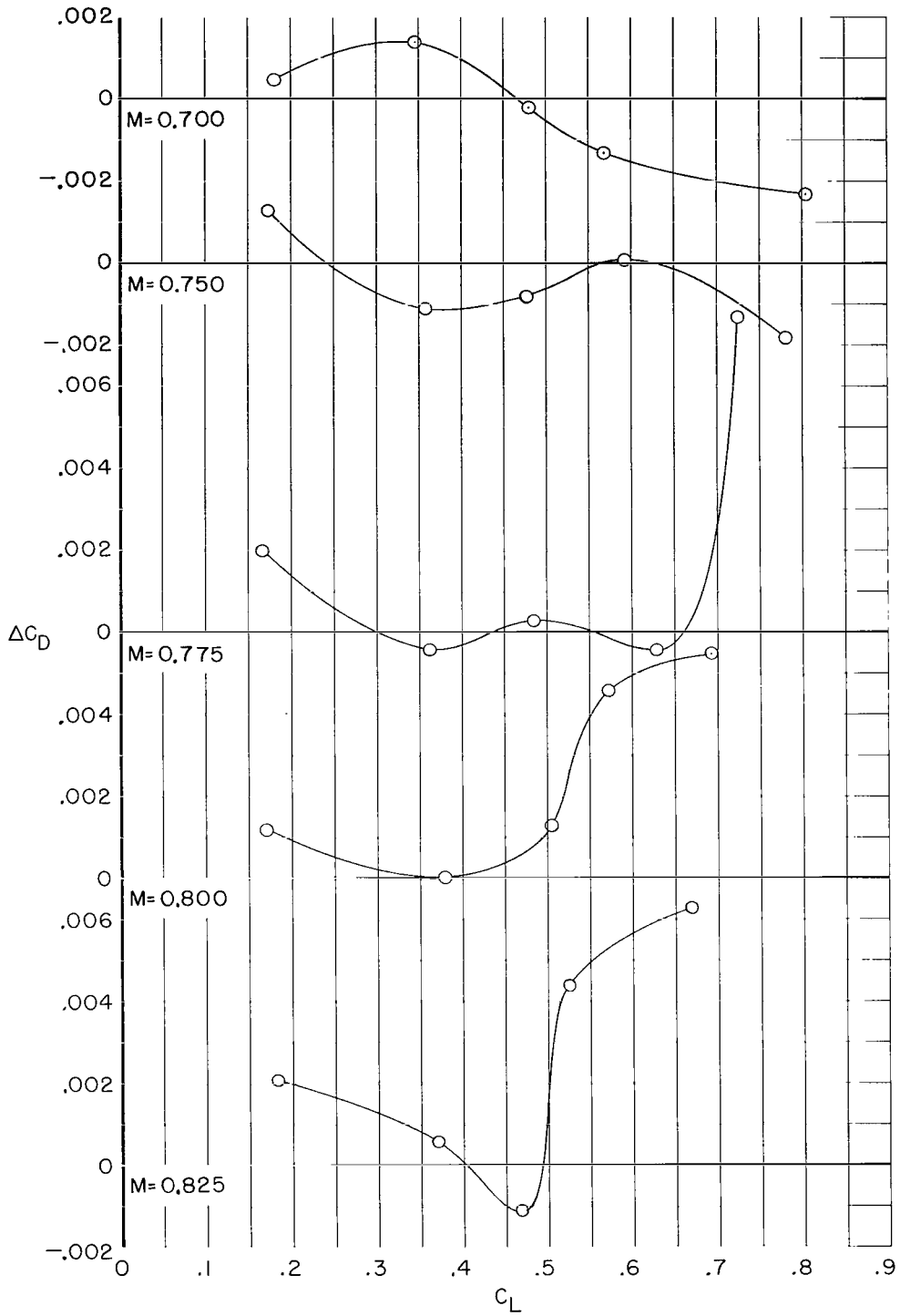


Figure 8.- Variation of aerodynamic-interference-drag coefficient with Mach number at a lift coefficient of 0.5 for six engine positions.  $p_{t,e}/p_{t,\infty} = 1.5$ .



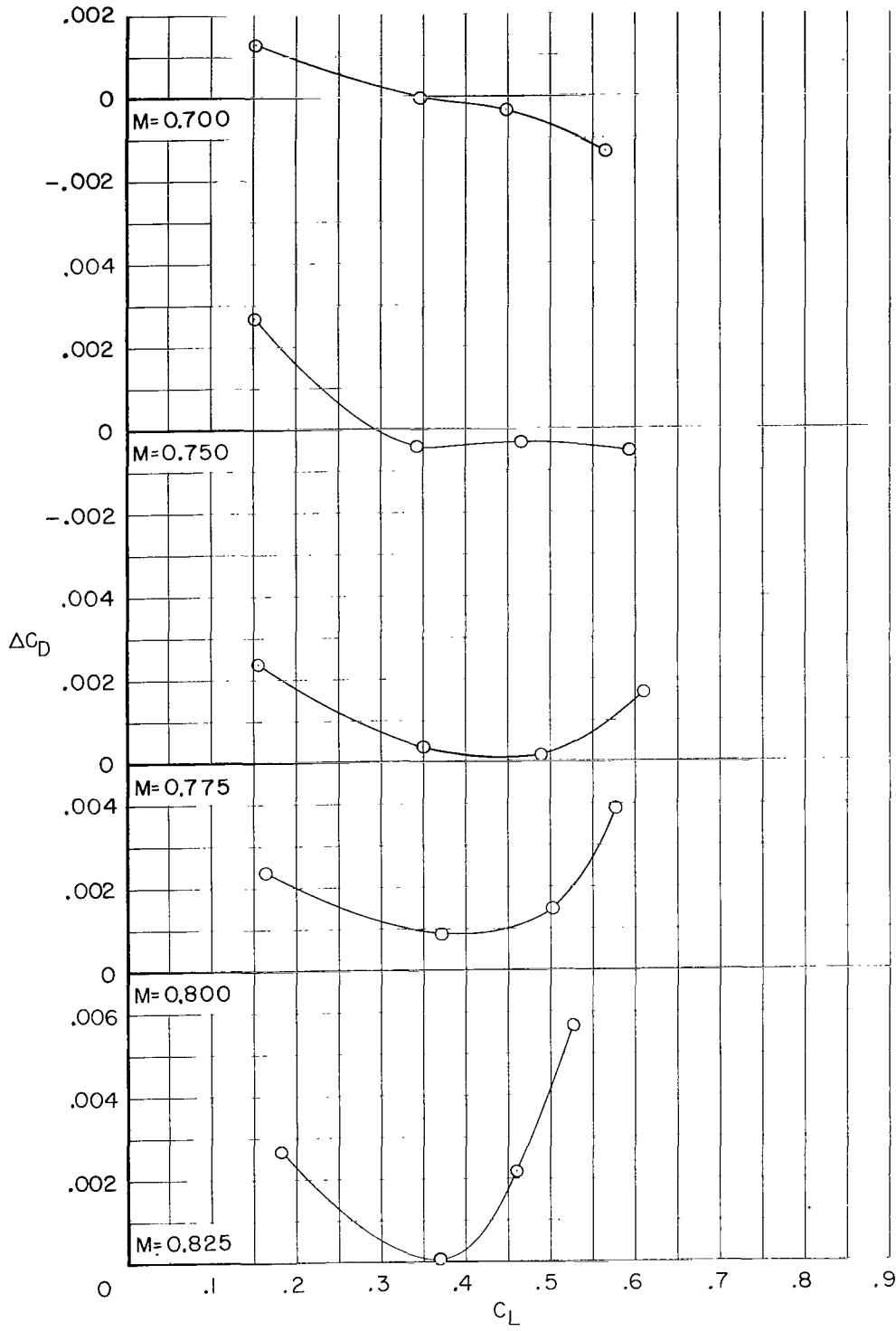
(a) Pylon 1.

Figure 9.- Variation of aerodynamic-interference-drag coefficient with lift coefficient of each test Mach number for each engine position, for the short- and long-duct flow-through nacelles, and for two spanwise engine positions.



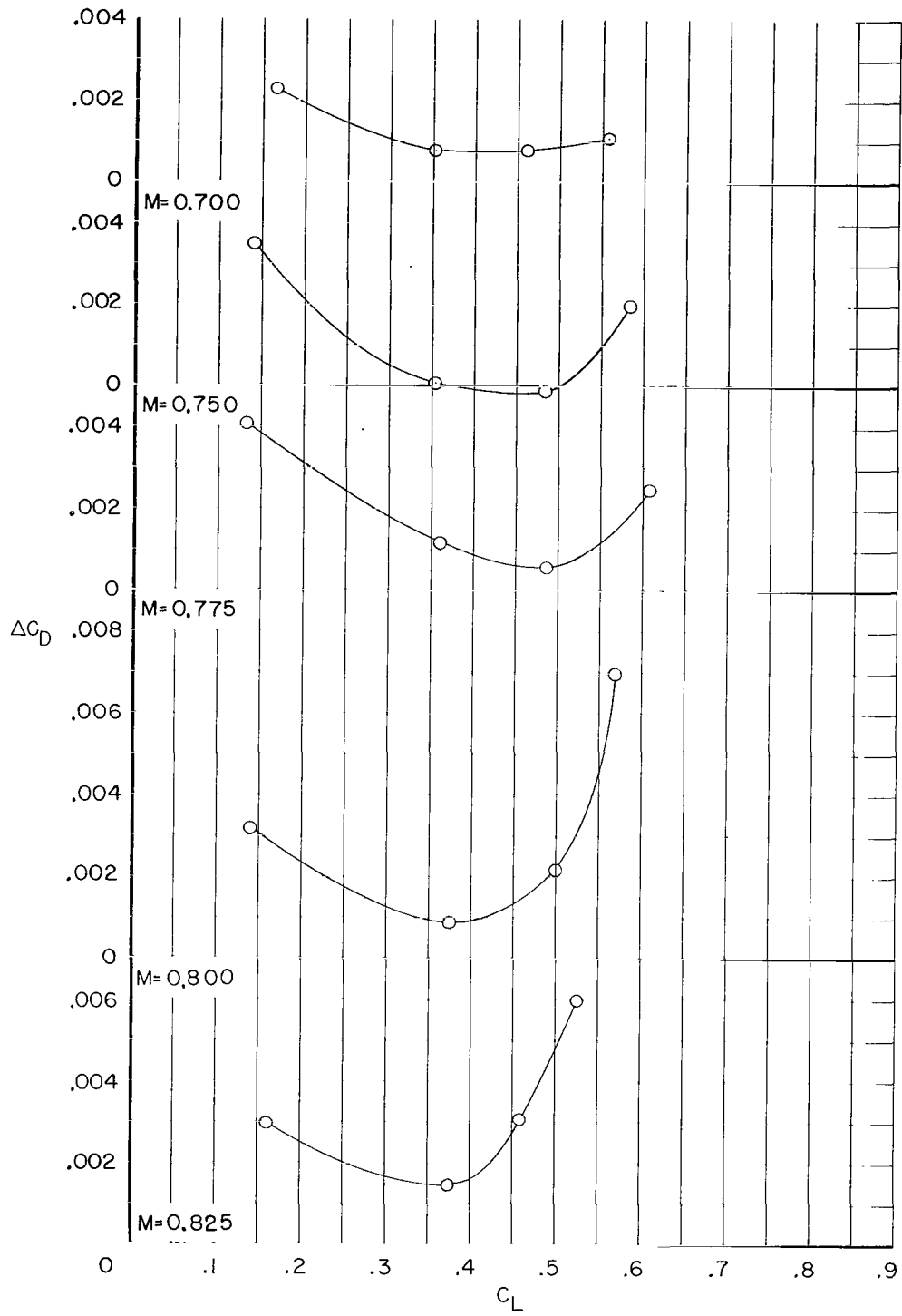
(b) Pylon 2.

Figure 9.- Continued.



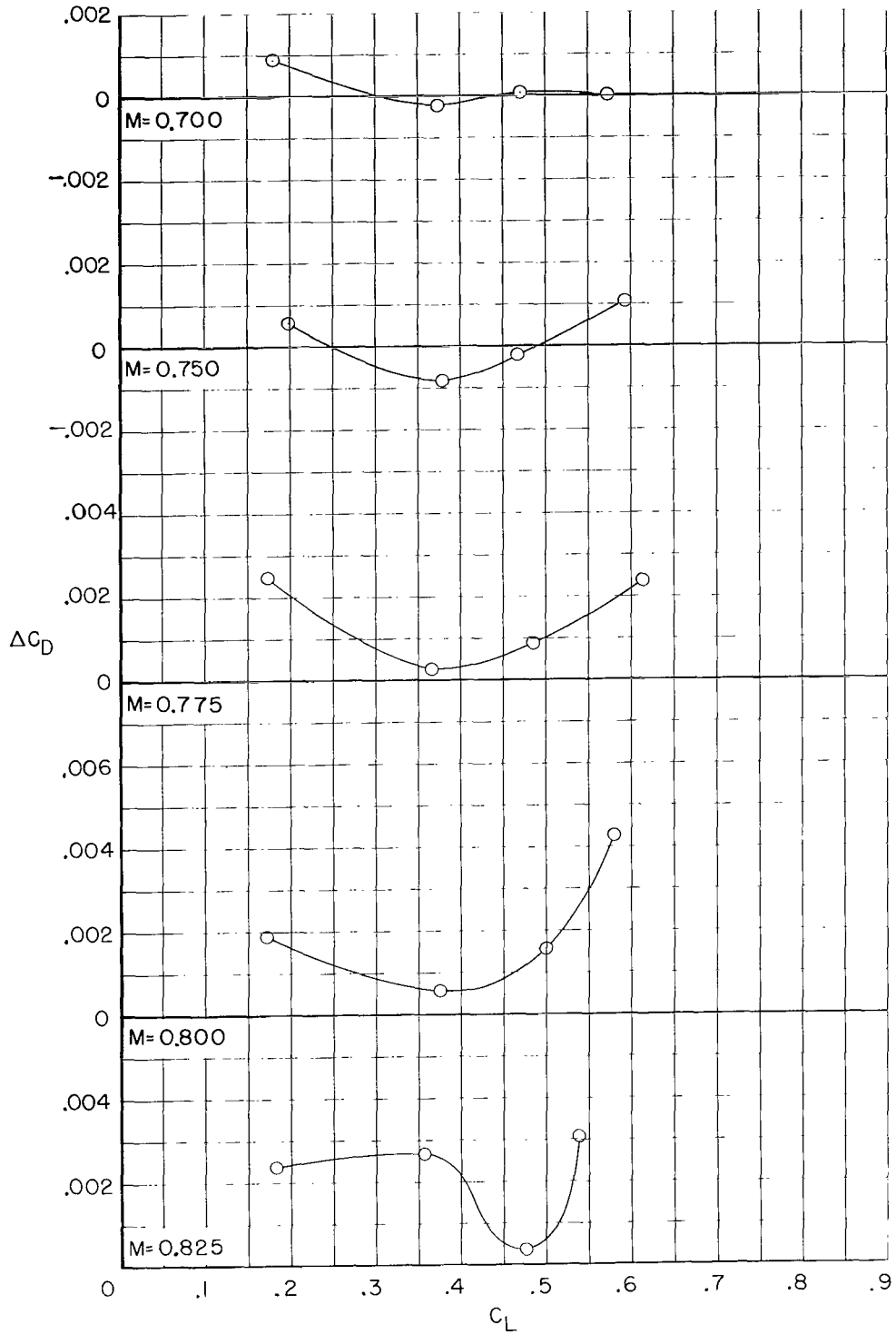
(c) Pylon 3.

Figure 9.- Continued.



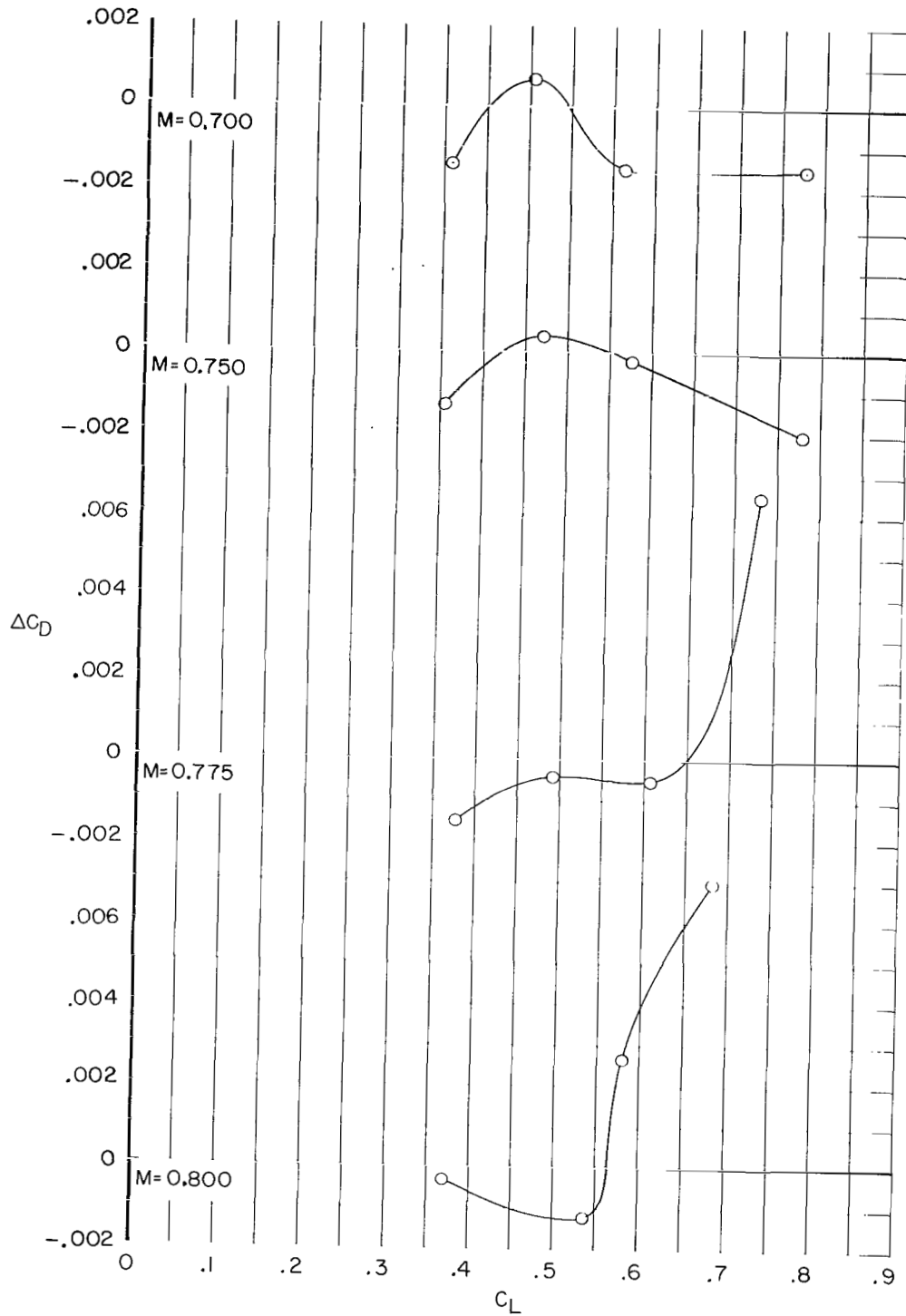
(d) Pylon 4.

Figure 9.- Continued.



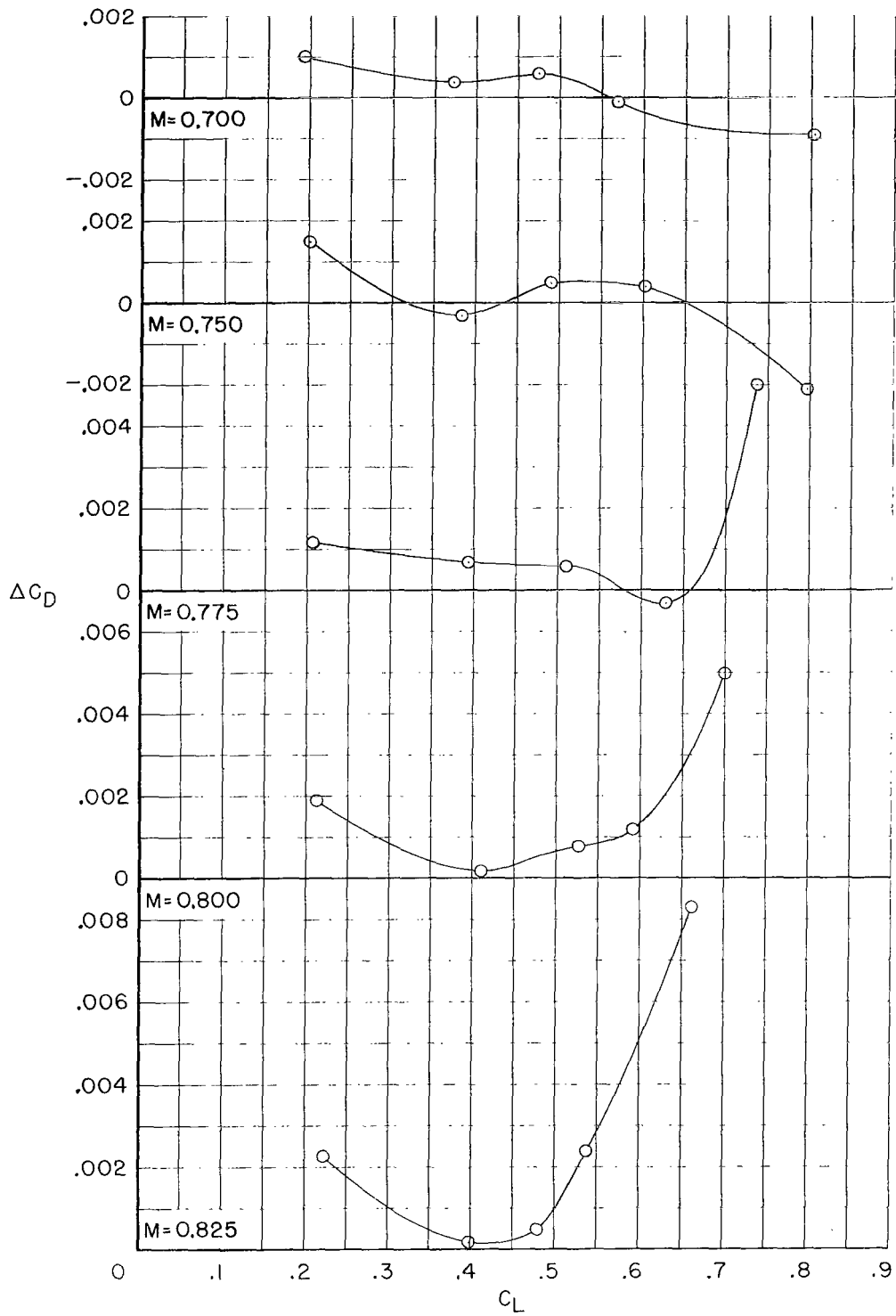
(e) Pylon 5.

Figure 9.- Continued.



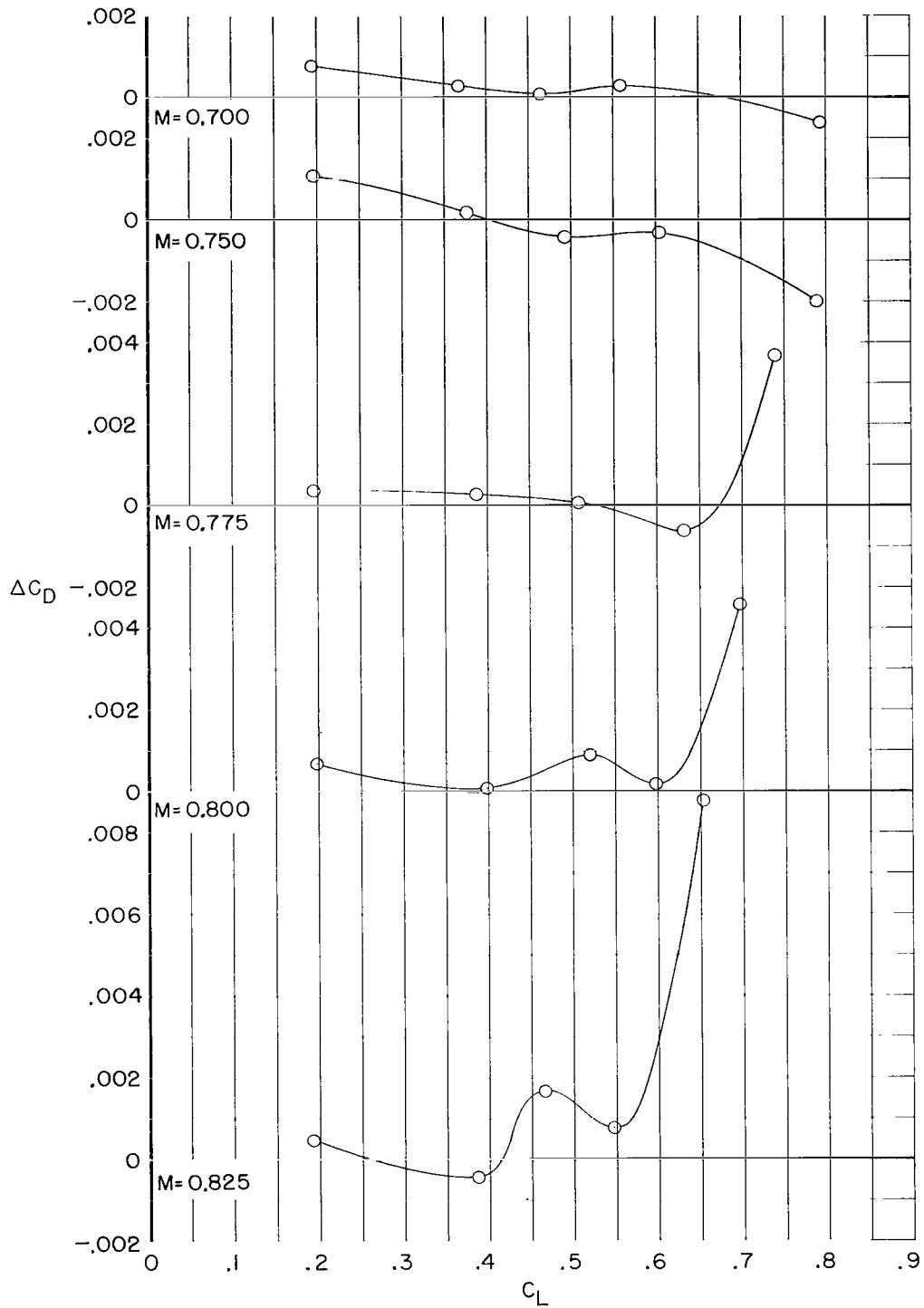
(f) Pylon 6.

Figure 9.- Continued.



(g) Short-duct flow-through nacelle.

Figure 9.- Continued.



(h) Long-duct flow-through nacelle.

Figure 9.- Concluded.

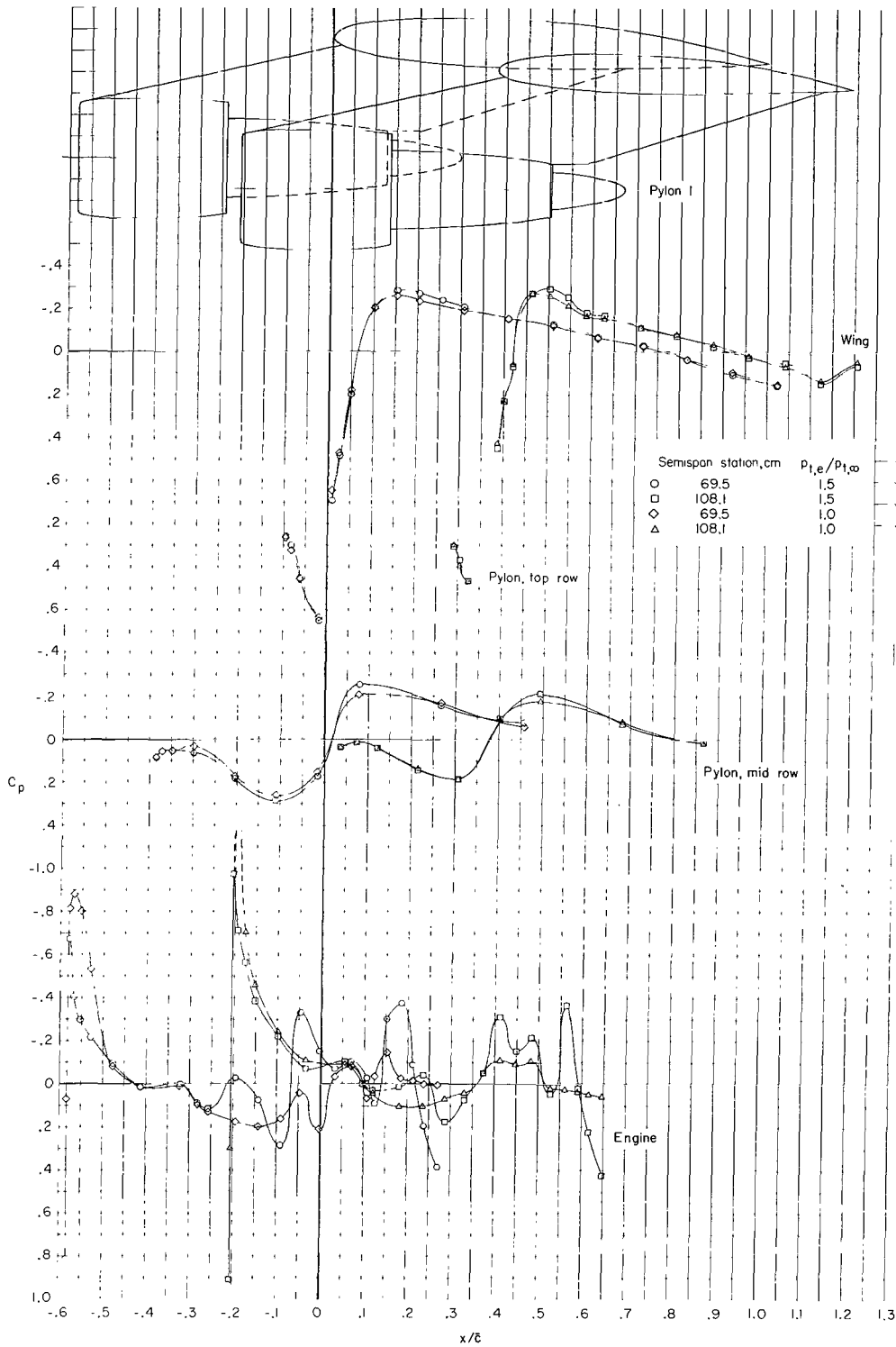


Figure 10.- Effect of power on pressure coefficients of wing lower surface inboard of each pylon, of pylon inboard surface of each pylon, and of engine surface inboard of each pylon.  $M = 0.75$ ;  $C_L = 0.5$ .

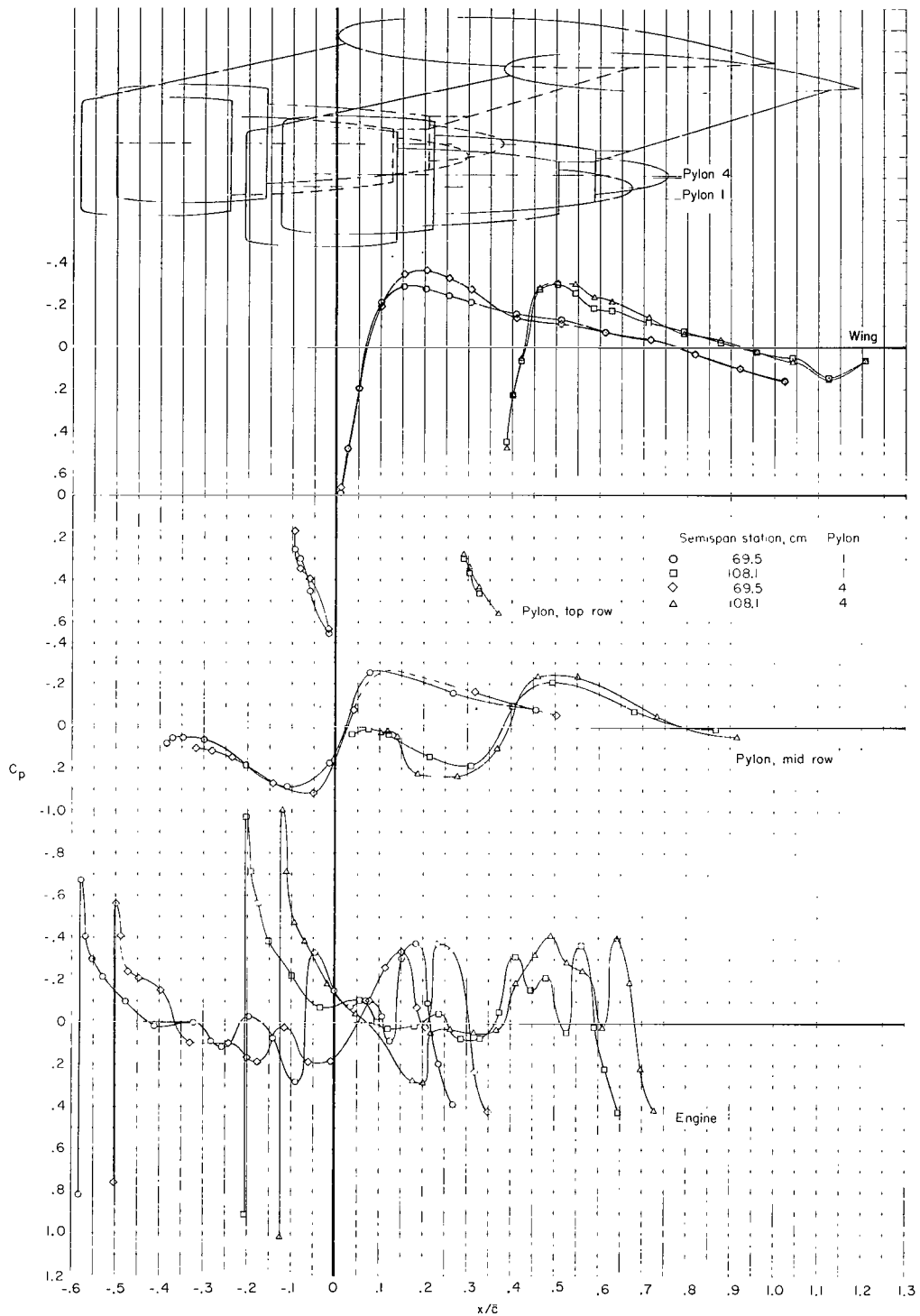


Figure 11.- Effect of engine position on pressure coefficients of wing lower surface inboard of each pylon, of the pylon-surface inboard of each pylon, and of engine surface inboard of each pylon.  
 $M = 0.75$ ;  $C_L = 0.5$ ;  $p_{t,e}/p_{t,\infty} = 1.5$ .

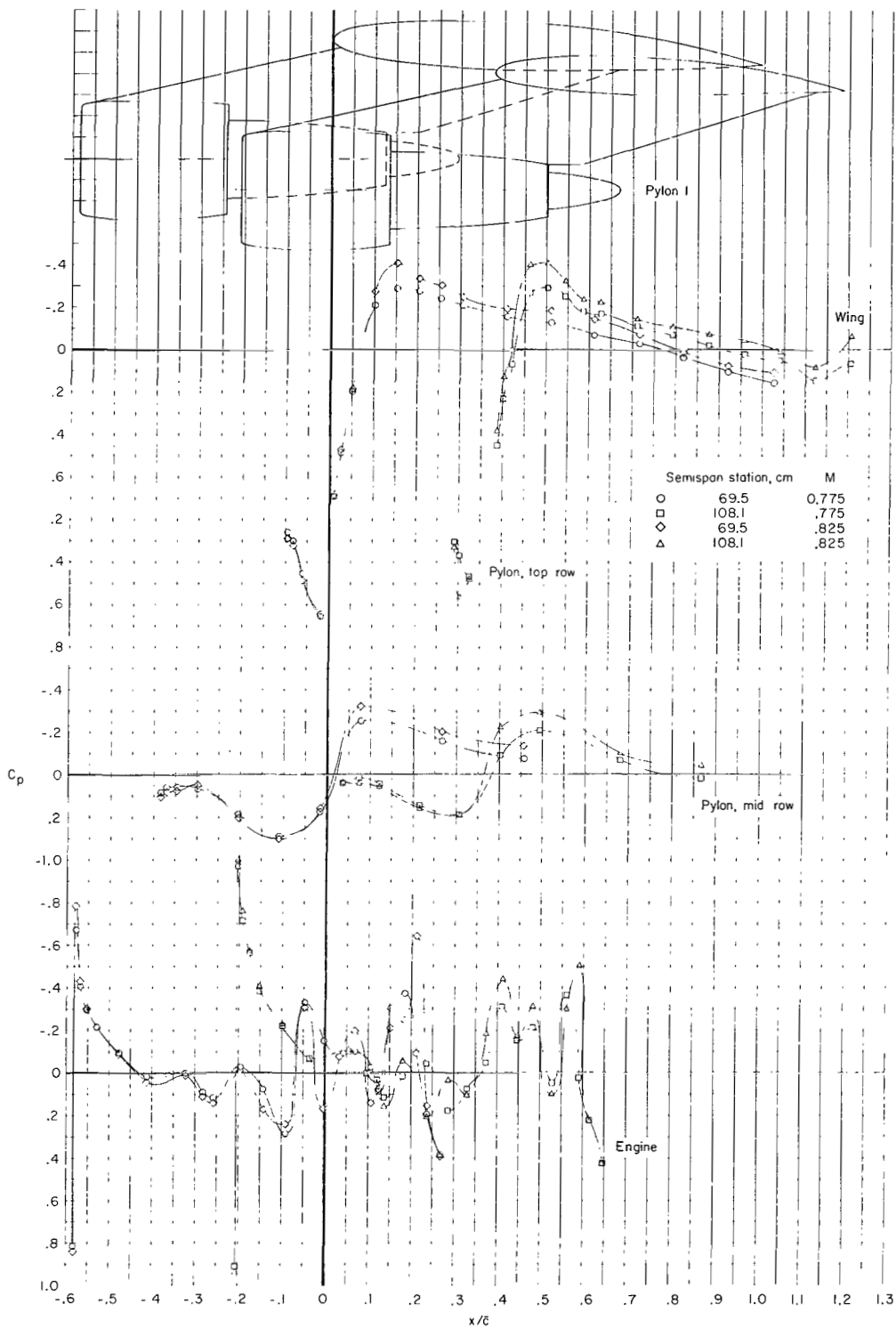


Figure 12.- Effect of Mach number on pressure coefficients of wing lower surface inboard of each pylon, of inboard pylon surface of each pylon, and of engine surface just inboard of each pylon.

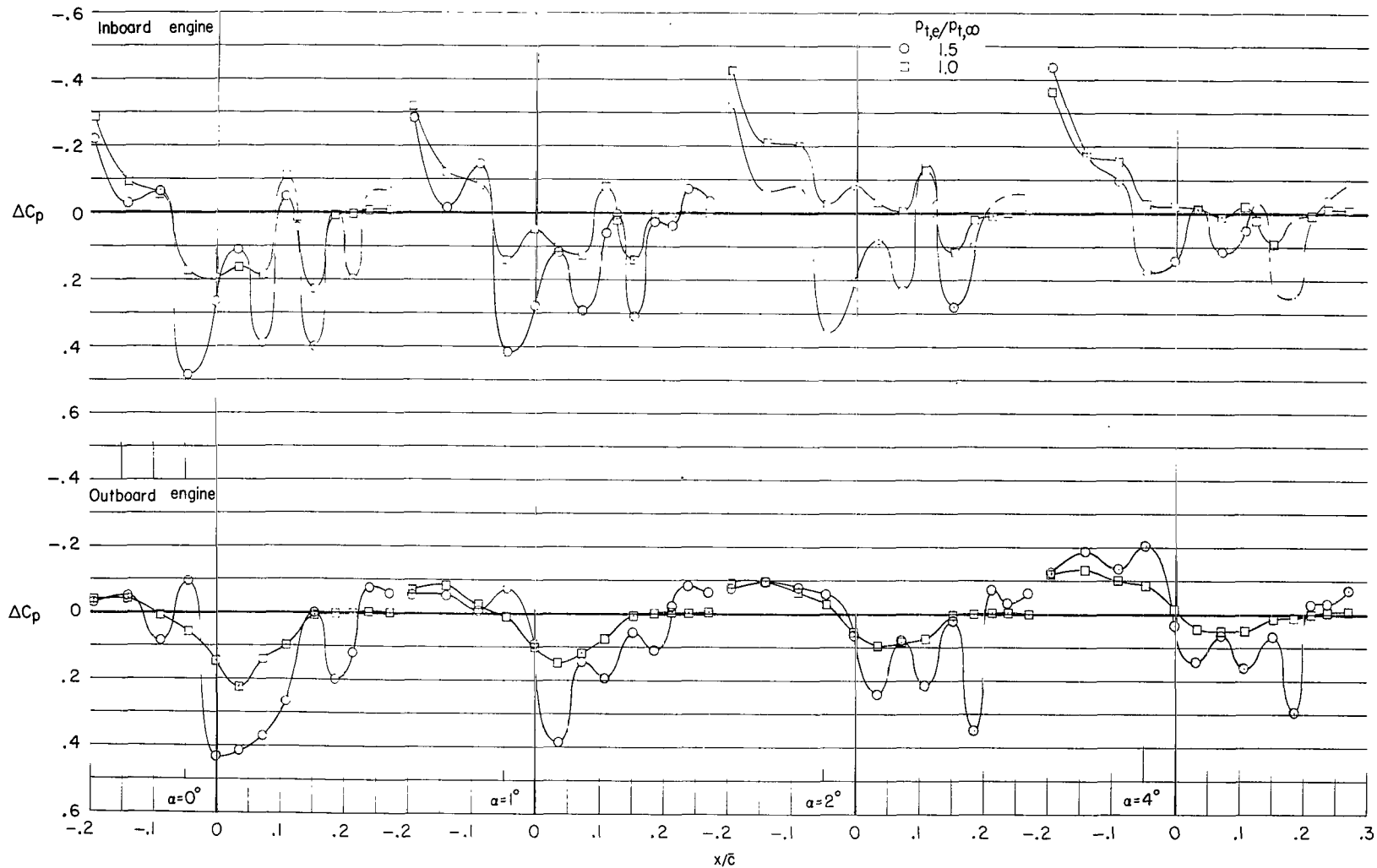


Figure 13.- Differential pressure coefficients of outboard and inboard surfaces of each engine at engine-pylon juncture presented as a function of longitudinal distance from wing leading edge in percent mean geometric chord.  $M = 0.775$ ; pylon 1.

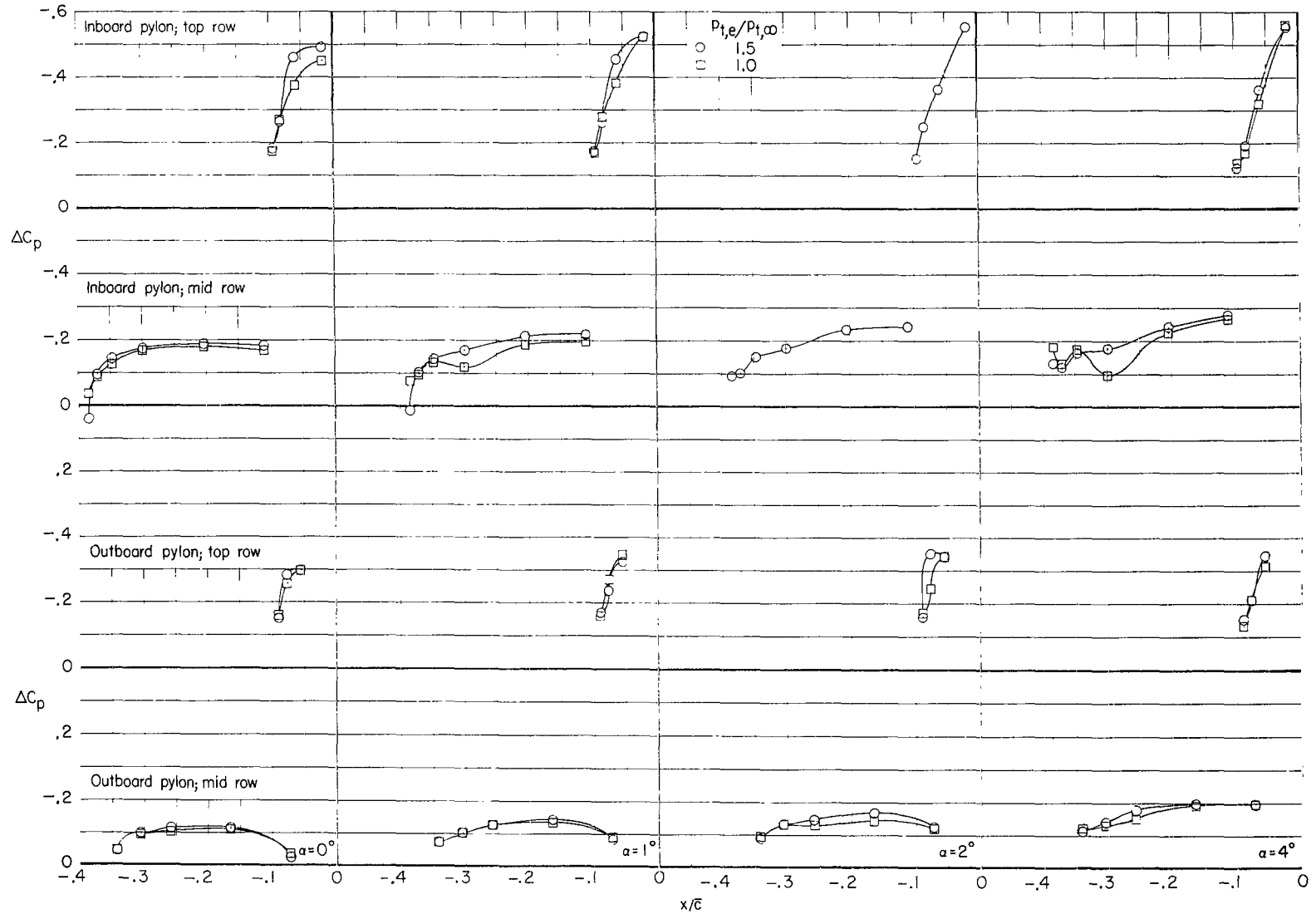


Figure 14.- Differential pressure coefficients of pylon measured at the pylon top and mid row locations presented as a function of longitudinal distance from the wing leading edge in percent mean geometric chord.  $M = 0.775$ ; pylon 1.

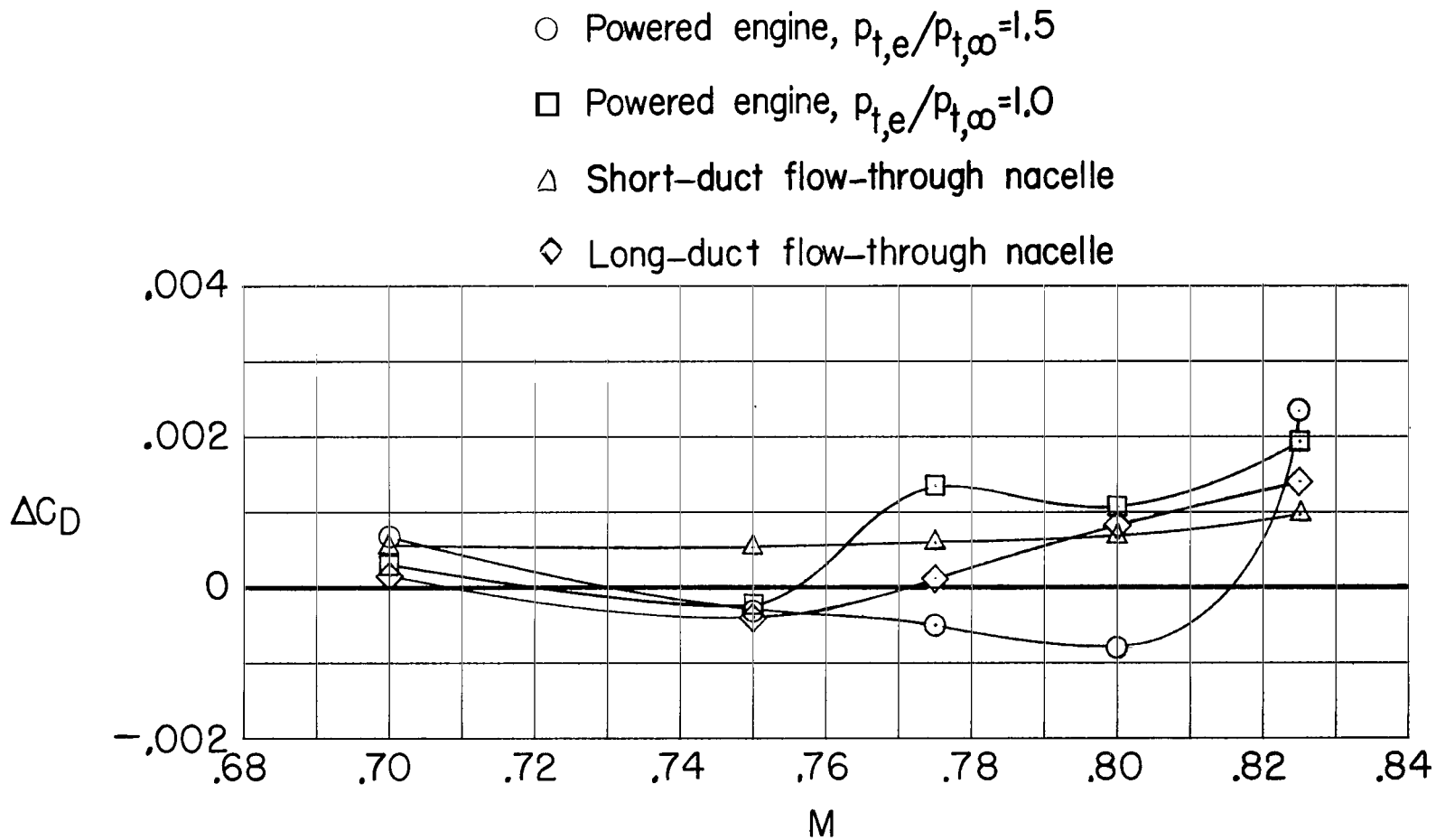


Figure 15.- Effect of flow-through nacelles on aerodynamic-interference-drag coefficient.  $C_L = 0.5$ .

FIRST CLASS MAIL



POSTAGE AND FEES PAID  
NATIONAL AERONAUTICS AND  
SPACE ADMINISTRATION

07U 001 26 51 3DS 70316 00903  
AIR FORCE WEAPONS LABORATORY /WLOL/  
KIRTLAND AFB, NEW MEXICO 87117

ATT E. LOU BOWMAN, CHIEF, TECH. LIBRARY

POSTMASTER: If Undeliverable (Section 158  
Postal Manual) Do Not Return

*"The aeronautical and space activities of the United States shall be conducted so as to contribute . . . to the expansion of human knowledge of phenomena in the atmosphere and space. The Administration shall provide for the widest practicable and appropriate dissemination of information concerning its activities and the results thereof."*

— NATIONAL AERONAUTICS AND SPACE ACT OF 1958

## NASA SCIENTIFIC AND TECHNICAL PUBLICATIONS

**TECHNICAL REPORTS:** Scientific and technical information considered important, complete, and a lasting contribution to existing knowledge.

**TECHNICAL NOTES:** Information less broad in scope but nevertheless of importance as a contribution to existing knowledge.

**TECHNICAL MEMORANDUMS:** Information receiving limited distribution because of preliminary data, security classification, or other reasons.

**CONTRACTOR REPORTS:** Scientific and technical information generated under a NASA contract or grant and considered an important contribution to existing knowledge.

**TECHNICAL TRANSLATIONS:** Information published in a foreign language considered to merit NASA distribution in English.

**SPECIAL PUBLICATIONS:** Information derived from or of value to NASA activities. Publications include conference proceedings, monographs, data compilations, handbooks, sourcebooks, and special bibliographies.

**TECHNOLOGY UTILIZATION PUBLICATIONS:** Information on technology used by NASA that may be of particular interest in commercial and other non-aerospace applications. Publications include Tech Briefs, Technology Utilization Reports and Notes, and Technology Surveys.

*Details on the availability of these publications may be obtained from:*

SCIENTIFIC AND TECHNICAL INFORMATION DIVISION  
NATIONAL AERONAUTICS AND SPACE ADMINISTRATION  
Washington, D.C. 20546